ABSTRACT

This study is investigating several spectral reflectance estimation methods: Wiener estimate, first-order Markov process and Gaussian Mixture Model. The object of the study is the eye fundus multichannel images. Wiener estimate and Gaussian Mixture Model demand representative training set of *a priori* data for the estimation, while first-order Markov process need only illuminant conditions and camera sensitivities to be known. The goal of the study is to compare and evaluate performance of the chosen methods.

Keywords: spectral reflectance, fundus, Wiener estimate, first-order Markov process, Gaussian Mixture model.

ACKNOWLEDGEMENTS

I would like to express my sincere thankfulness to people who supported me during my studies and research work. My special and sincere gratitude to Professor Jussi Parkkinen, Vice Rector of the University of Joensuu, Finland, for the opportunity to participate in IMPIT program and to continue my studies even after 6 month of forced absence. Your personality, strength and wisdom are exemplar for me outside of a classroom as well.

I would like to sincerely thank Dr. Markku Hauta-Kasari, Director of InFotonics Centre, Joensuu, for the ability to join the wonderful team and for his kind guidance during my research work.

My warm thankfulness to Ville Heikkinen for his endless patience and helpful discussions on different topics, especially my thesis.

I would like to thank Ph.D. Alexander N. Kolesnikov for his great help during my studies and especially for his high availability for discussions anytime.

I would like to thank every single person from Color Research Group for feasible help and collaboration.

I would like also to denote my special thanks to all my friends, especially kazakh ones, for their support and inspiration at all times.

At last, but not the least, I would like to express my deepest love and thankfulness to my family and relatives, and especially to my grandmother Valentina and my sister Elena for all sacrifices made for me and for support that could not be overestimated.

University of Joensuu

Department of Computer Science

Master's Thesis

Estimation of Human Fundus Spectral Reflectance from Multichannel Measurements

Alessya Gorelova

Supervisors:
Dr. Markku Hauta-Kasari
MSc. Ville Heikkinen

September, 2009

TABLE OF CONTENTS

Chapter 1

INTRODUCTION

1.1 Overview

Color is the one significant feature in digital imaging. The accuracy of object's color representation has significant affect on research results in many applications for printing, digital recording and archiving, medicine, e-commerce, and others based on digital color imaging.

A spectral image represents spectral information – electromagnetic radiation reflected or transmitted from an object. It may contain hundreds of components in some wavelength range corresponding to samples from different spatial locations of the object. This representation is highly informative, and can eliminate the effect of illuminant and provide access to device independent color spaces.

A multichannel image consists of 1 to 10 image components or channels. Widely used RGB cameras are based on the physiology of a human eye and have only three channels for image capturing. Thus conventional thrichromatic cameras quantize the whole spectral information into three channel color image. In this case the representation of color information is illuminant and device dependent. RGB images are fast to capture measurements and imaging is easy because of high mobility of camera.

Spectral image acquisition is time consuming and expensive when compared to multichannel imaging, and therefore, researchers are looking for techniques of

estimating spectral information from multichannel measurements [5-7; 13; 14; 20; 22; 24; 29].

1.2 Work Description

Since 1950 some researchers attempted to study light reflected by the eye fundus both in spatial and in spectral spaces [1]. Development of new spectral and fundus cameras facilitated studying a fundus reflectance for different purposes. Researchers measure and identify druses in age-related macula degeneration, study macula, properties of crystalline lens, age related changes and pigments distribution, attempt to investigate and diagnose diabetic retinopaty, glaucoma, myopia and other eye diseases [1; 2; 23; 27; 32].

The *aim* of the study is to investigate the estimation relatively to computational cost and quality for fundus images. The estimation of reflectance from multichannel camera responses decreases the speed of spectral reflectance image acquisition. Obtained spectral estimates can be further used for the purposes of medical analysis.

Spectral reflectance images of fundus, measured by the InFotonics Center, Joensuu [10] were used for the current work. Real multichannel images were not used, but multichannel fundus images were simulated from the spectral reflectance images under assumption of known illuminant, noise distribution and camera characteristics.

Three standard estimation methods were used in this study. Multichannel images were simulated from reflectance data using Gaussian functions for different channels and chosen methods were examined in order to identify possible differences in the fidelity and input data requirements for the estimation. Initial requirements for the methods deviate significantly, and it is important to define the minimal amount of the information to be extracted in order to provide eligible fidelity of the estimation.

The thesis concepts are presented as follows. Chapter 2 provides an introduction to the objects of the study: light and color, structure of the human eye, specifics of the RGB and spectral imaging techniques.

Chapter 3 will help the readers to get familiar with methods used to estimate spectral reflectance in current study. Chapter 4 provides a description of the experimental part of the study. It contains the detailed description of the used dataset, simulation settings and evaluation of the estimations by each of chosen methods with fidelity criteria. Chapter 5 summarizes experimental results and presents conclusion of the study with possible suggestions of improvement.

Chapter 2

FROM LIGHT TO IMAGE

2.1 Light and Color

Everything from clothes to leaves on the trees has a color. And that makes the world a beautiful place. But how does the color sensation work and what are the components of it?

Number of objects in our environment, like stars, lamps, laptops, ovens and many of natural objects, emit streams of photons producing electromagnetic radiation waves of different wavelengths. Figure 2.1 represents wavelength ranges of the electromagnetic radiation.

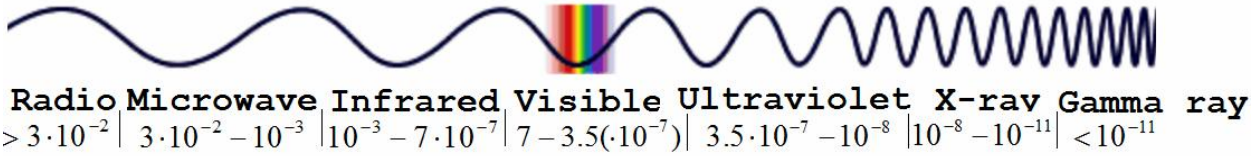

Figure 2.1. Electromagnetic spectrum of electromagnetic radiation with corresponding wavelengths.

It is obvious that people deal with electromagnetic radiation every day when waking up in the morning and seeing the sun from the window, listening to music on the radio, using microwave oven to warm our food, walking in the forest in the afternoon, reading news on the laptop, turning on the floor lamp to read a book in the evening, doing X-ray photograph or tomography in the hospital, shooting home

video from the birthday, going to the bank to put money to the bank account. Indeed, the electromagnetic radiation is all around.

Visible light is defined to be a part of the electromagnetic radiation in range of wavelengths from 380 to 780 nanometers perceptible and detectible by a human eye [31]. Imaging in visual light is what human is used to deal with in everyday activity. Figure 2.2 illustrates process of human color perception.

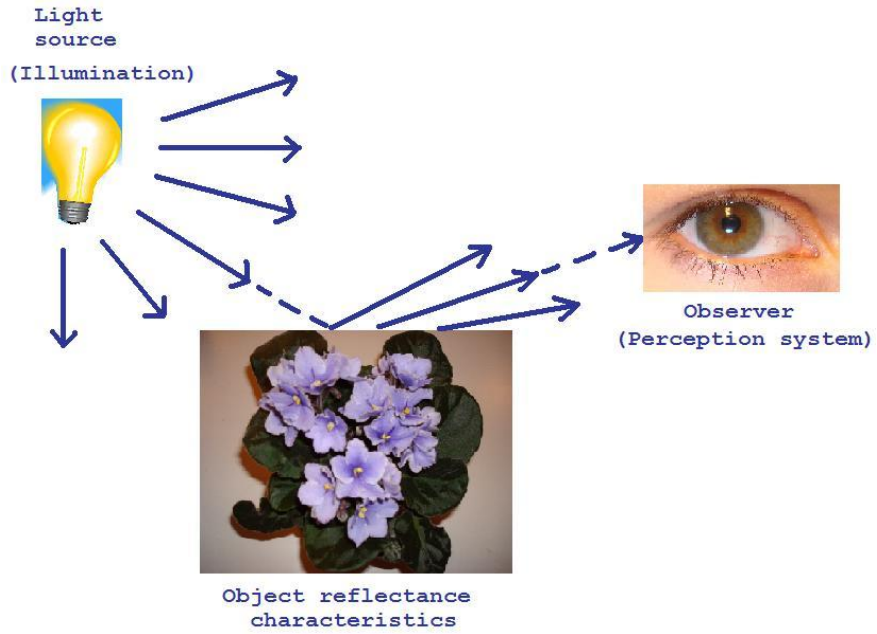

Figure 2.2. Process of human color perception.

According to [9] *illuminant* is a light source that has been measured or specified formally in terms of spectral energy. The CIE International Commission for Illumination has specified a number of CIE standard illuminants differing with their spectral power distribution. Most popular CIE illuminants are [9]:

- Illuminant A – a tungsten light source;
- Illuminant D – various models of daylight (D50, D55, D65, D75);
- Illuminant F – various models of fluorescent light (F1-F12).

In the current study all the spectral measurements and simulations were done using D65 standard illuminant. Spectral power distribution of the illuminant is presented on Figure 2.3.

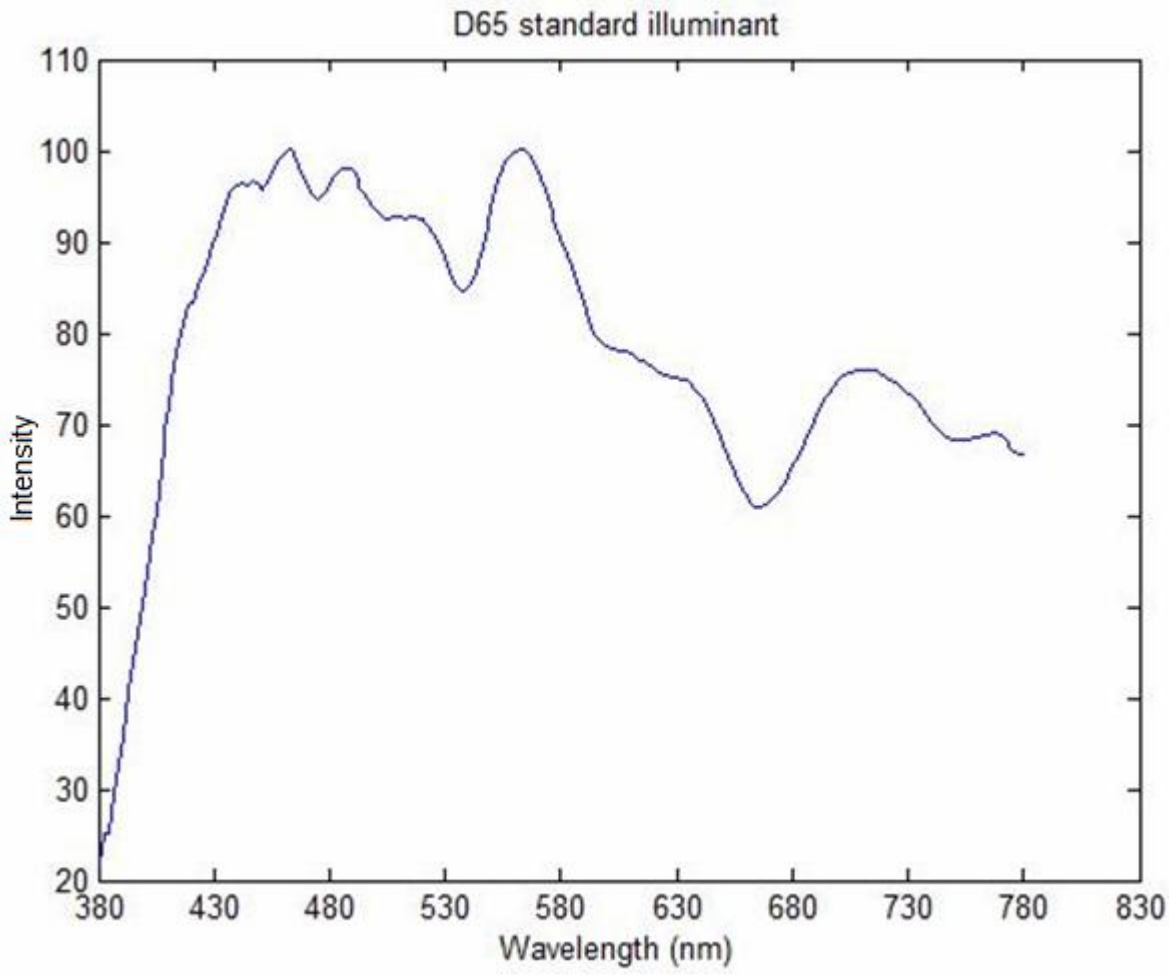

Figure 2.3. D65 standard illuminant spectral power distribution.

In the XVII century Newton suggested that surfaces absorb radiation in some wavelength range and reflect others. But the color is not a property of object. It is our perception of the reflected visible light [31]. The final signal is a combination of reflected radiation and illumination which propagates to imaging system. Figure 2.4 illustrates human perception of visible light depending on the wavelength.

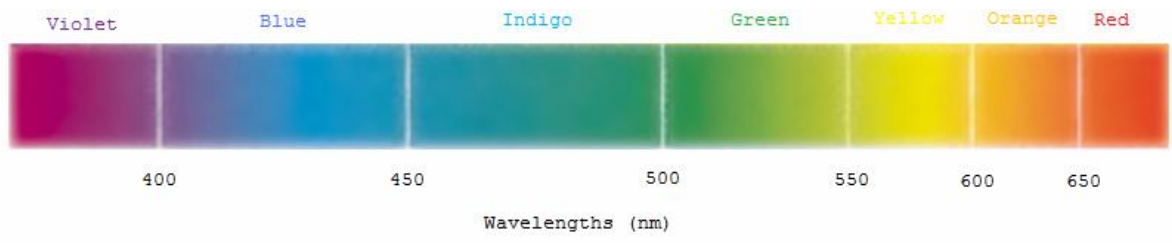

Figure 2.4. Visible light.

2.2 Human Vision System

Human color perception is a physiological process depending on the condition of human eyes (see Figure 2.5) and brain. Therefore the colors that human sees are unique and there is no two people who would see the color exactly the same.

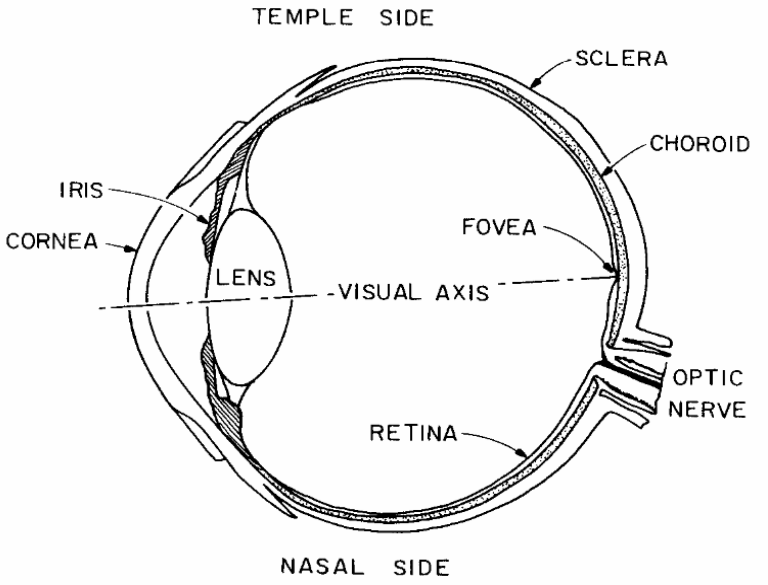

Figure 2.5. Structure of human eye [21].

Human eye together with brain receives visible spectrum of light and translates it into perception of color as shown in Figure 2.4. The question arises “How it happens?”

When a person perceives visual information, the portion of light, measured by the *iris*, comes through transparent *cornea* from the environment and focuses onto the *retina* by the *lens*. The retina itself is a part of brain and it is covered by millions of light-sensitive receptors – *cones* and *rods.* Cones and rods process the light into the nerve impulses and pass them to the brain via the *optic nerve* [21; 31].

Cones are color sensitive receptors with different absorption characteristics as function of wavelength with peak in red, green or blue part of visible spectrum. Thus human vision system can not distinguish particular wavelengths of light [11]. Most of the cones are located in the central part of retinal *macula*, called *fovea*. Human sees colors because of the *photopic* (or bright-light) vision provided by

cones. Figure 2.6 illustrates typical absorption characteristics of the cones. Curves indicate what *a* cones, responsible for blue light perception, have low sensitivity relating to others [21]. The existence of these types of cones and their curves overlapping provided a physiological basis of the thrichromatic theory of human color vision and prevalence of RGB imaging [28].

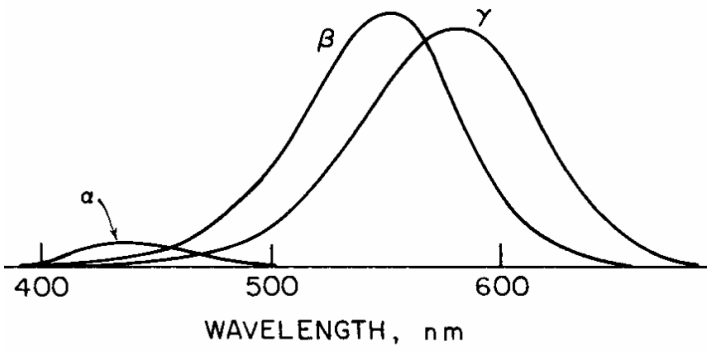

Figure 2.6. Spectral absorption curves of cones of human retina [21].

Number of rods is significantly larger – they cover almost all retina surface. *Rods* are sensitive to low levels of illumination. They provide general picture of the environment. The rods provide human's ability to see colorless shapes of objects in the night time, when one uses the *scotopic* (or dim-light) vision [11].

It is really hard to misjudge the importance of the retina functionality in our life. And it makes the experimental part of this study more interesting since investigation in this study will be done for the images of human eye fundus.

2.3 RGB Color Space and Imaging

The aim of *color model* is to describe colors in some general way. Most of the color models are oriented toward hardware or toward color manipulations. Among hardware oriented models the most practically used are RGB (red, green, blue) for displaying and CMYK (cyan, magenta, yellow, black) for printing. Among the

color graphics and animation oriented mostly used models are HIS (hue, saturation, intensity) and HSV (hue, saturation, value) models [11].

Current study is based on simulated camera responses. It is assumed that these camera responses can be approximately transformed to RGB space (RGB). Here is some brief description of the RGB space, one of color space used in imaging.

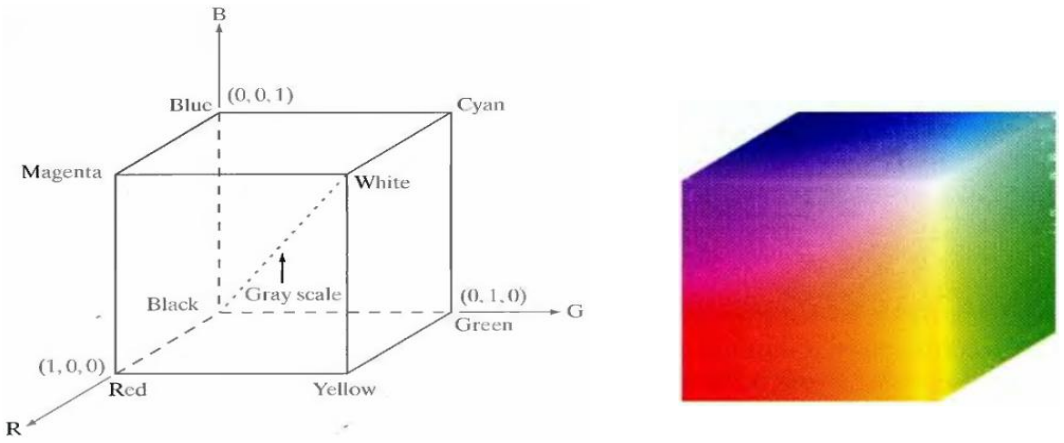

Figure 2.7. RGB color cube.

RGB color model is additive, meaning that it operates with light emitted from a source. Red of 700.0 nanometers, Green of 546.1 nanometers and Blue of 435.8 nanometers lights are so called *primaries* of the RGB color space. All others of more then 16 million colors can be obtained by combining different amount of red, green and blue light. All colors can be presented in the so called *RGB color cube*, shown in Figure 2.7. All values of red, green and blue are assumed to be normalized in the range [0,1]. Black color means that no light is added. Combining all primaries in an equal amount produces white color. Thus the main diagonal of the cube represents shadows of grey and indicates direction of lighter colors. Combining each two of primaries in an equal amount produces *secondary primaries* – cyan, magenta and yellow colors [11; 21; 28].

RGB model can be called a basic color model because other color models like CMYK, YIQ, HIS, HSV can be obtained from RGB model through relatively simple computations. Formulas for the conversion can be found for example in [11; 28]. Images in the RGB model consist of three independent primary color image

planes. Figure 2.8 illustrates representation of the RGB images and also introduces the image of a human fundus mentioned in the Section 2.2.

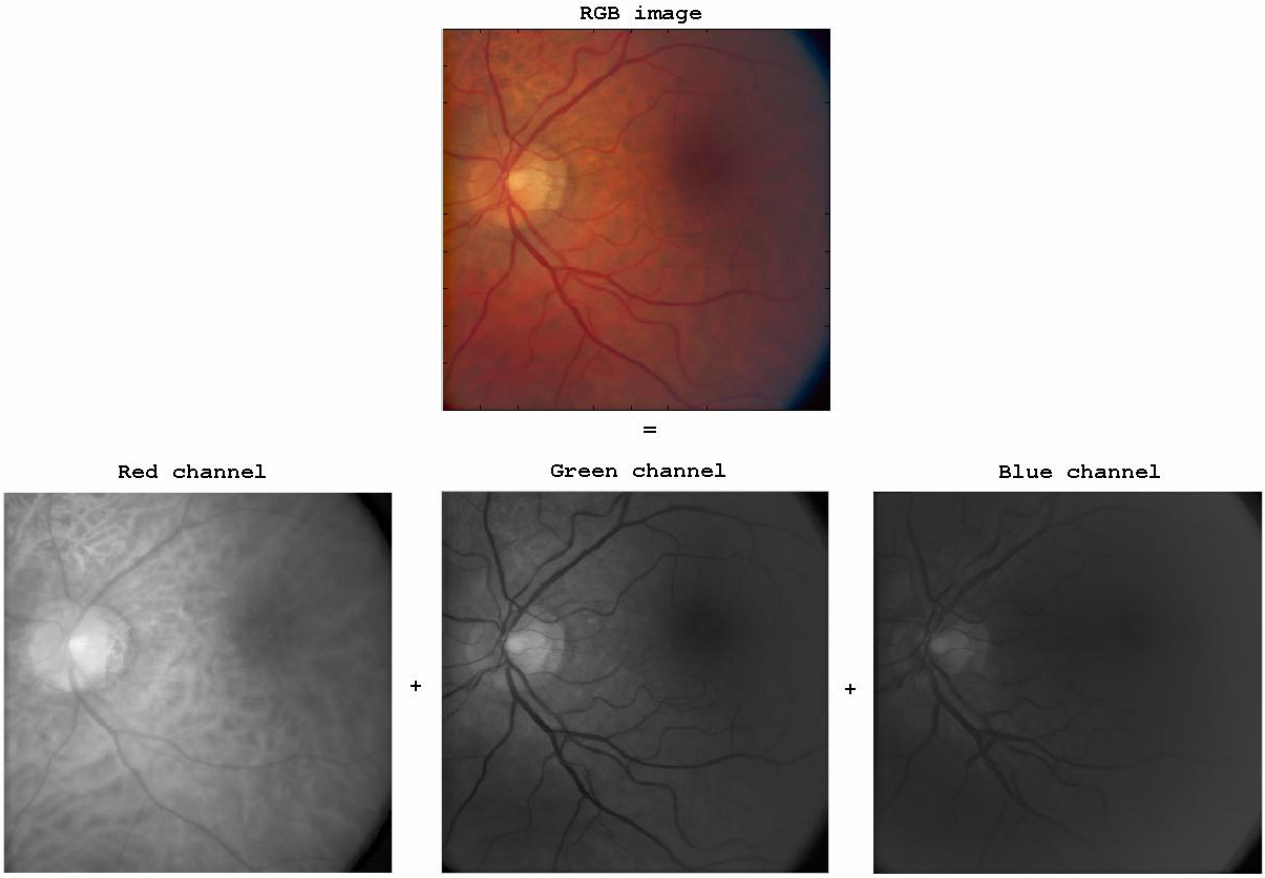

Figure 2.8. RGB image of a human fundus.

Since this model is comparatively easy and cheap to implement into hardware, the RGB color model became the most utilized way of gathering and reproducing color images in monitors, digital and video cameras, scanners. For example, computer monitor screen consists of hundreds of red, green and blue phosphor dots. These dots are activated electronically to emit light, thereby combination of different intensities from the dots produces color image on the screen. Digital cameras have thrichromatic matrices to gather amount of red, green and blue from the object of photography.

The *advantages* of the RGB model are obvious: the model provides fast capturing of the image; RGB images are relatively small and fast to process; due to the human vision characteristics RGB imaging provides good colorimetric match to

natural objects. At the same time the *disadvantages* of the RGB object representation are strong as well. Once someone holds image acquisition process under illumination, the effect of it can not be eliminated. Thus if the illuminant is changed, the only way to obtain new RGB image is to repeat image acquisition process, restricted to visual wavelength range.

Another problem is the effect of *metamerism*. In practice it means that either the number of channels, or the spectral sensitivity properties of the individual channels in the system are so poor, that two surfaces with different spectral color characteristics can look the same under one set of conditions and different under another set of conditions.

2.4 Spectral Imaging

Spectral reflectance is an accurate representation of the surface characteristics and it is independent of illuminant. Spectral imaging approach measures object surface spectral reflectance using high number of channels with high spectral resolution, extending information content not only in the visible wavelength range, but also in the ultraviolet (UV) and infrared (IR) range.

Some of the *advantages* of this approach are that reflectance information of the object itself allows reproducing image of the object under any illumination, for any observer, under any sensitivity characteristics of the camera and in any of the color spaces. The approach also allows avoiding the effect of metamerism and multiple iterations of the new image acquisition, providing significantly higher information content comparing to multichannel data. This approach represents true color of surfaces and provides high-fidelity color reproduction of objects. Spectral reflectance image can be viewed directly, using pseudo-coloring of same wavelength areas or using conversion to some color space, like RGB mentioned in Section 2.3, under some chosen illuminant.

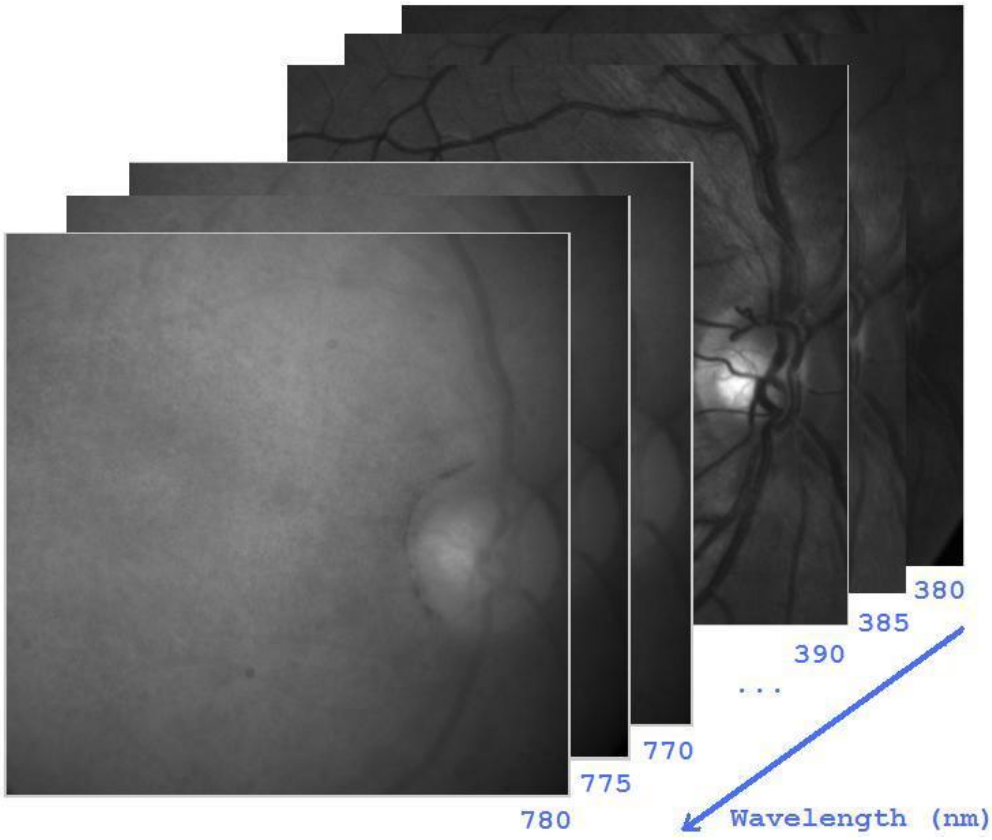

Figure 2.9. Spectral image of human fundus.

Figure 2.9 illustrates typical spectral image. Each spectral image corresponds to a certain wavelength of visible spectrum range from 380 to 780 nanometers in 5 nanometers sampling. Thus, unlike in thrichromatic imaging systems, spectral imaging system usually uses tens or hundreds of spectral channels in the visible range to capture the radiance reflected from the surface.

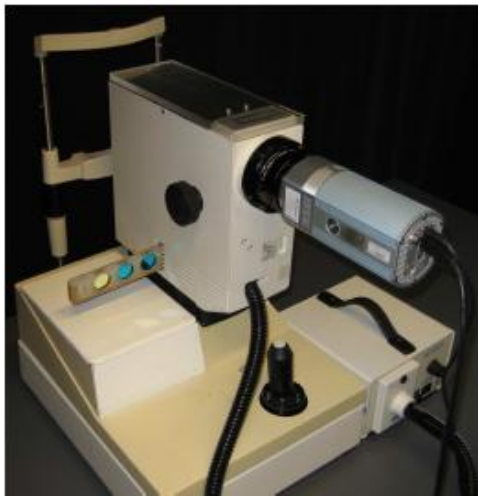

Figure 2.10. Fundus camera based spectral imaging system [10].

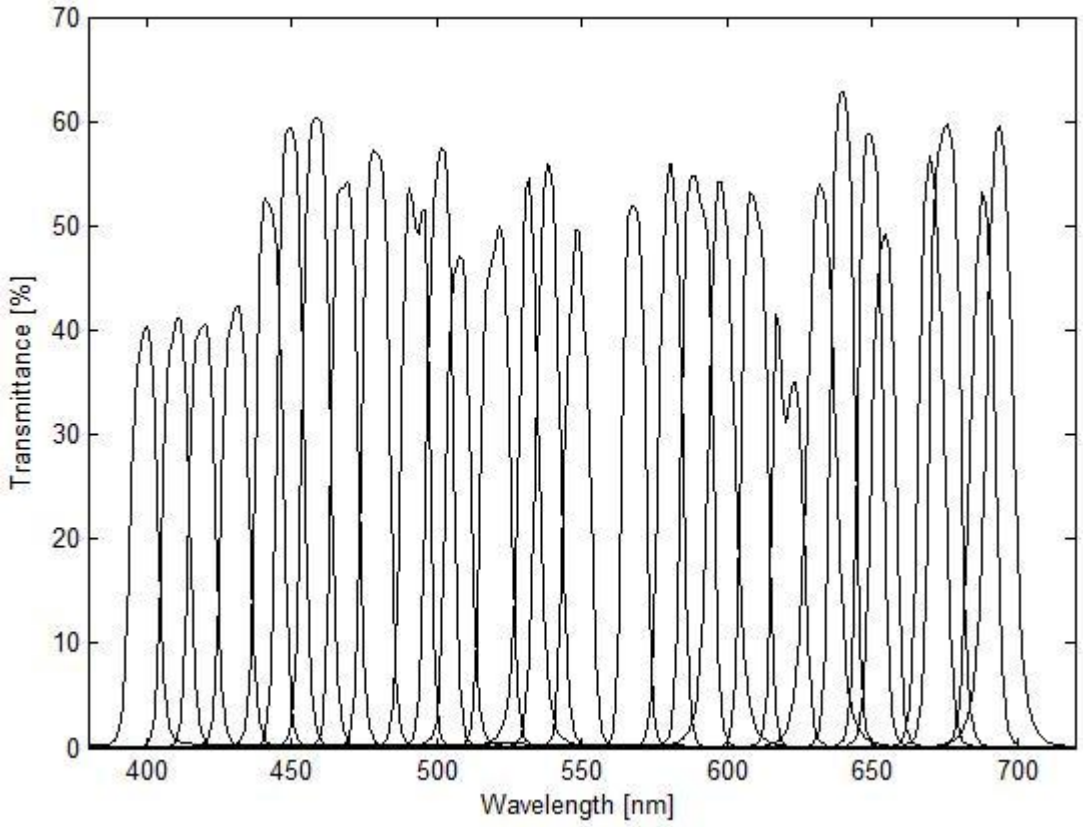

Figure 2.11. Spectral transmittance of interference filters [10].

Eye fundus spectral image acquisition demands modified fundus camera system to be used. *Fundus camera* is an optical tool based on low power microscope and digital camera, and designed to investigate interior surface of the eye [4]. Figure 2.10 presents fundus camera based spectral imaging system [10] constructed in the InFotonics Center, Joensuu and used for capturing retinal spectral images. The modified fundus camera was made of basic fundus microscope optics with attached digital monochrome CCD (Charge-Coupled Device) camera and interference filters. Spectral transmittance of used filters is presented on Figure 2.11.

Following explanation will briefly present details of obtaining reflectance images from spectral imaging system responses. Response c_i of the image capturing system for i^{th} channel is approximated as:

$$c_i = \int s_i(l)l(l)r(l)dl + n_{i0} \quad , \tag{2.4.1}$$

where $s_i(l)$ is the channel characteristic of the i^{th} camera channel; $l(l)$ is the spectral power distribution of the illuminant; $r(l)$ is the spectral reflectance of the

object; n_{i0} is additive noise for i^{th} capture; $i=1,..,n$ and n is the total number of camera channels. It is assumed in this study that the channel's characteristic is a combination of additional filter's sensitivity and all other functions in the optical path.

Further it is assumed that in an ideal case $s_i(l)$ corresponds to shifted Dirac delta function $d_i(l) = d(l - l_i)$ [3] and the noise-free spectral camera responses are:

$$c_i = \int s_i(l) l(l) r(l) dl = l(l_i) r(l_i), \tag{2.4.2}$$

The ideal white reflectance (reflectance value equal to 1) can be approximated as:

$$w_i = \int s_i(l) l(l) dl = l(l_i), \tag{2.4.3}$$

Then the reflectance r can be obtained as:

$$r = \frac{c}{w}, \tag{2.4.4}$$

where the division is made point-wise.

Approximation for further derivation of relationship between spectral input signals and sensor responses c can be written in matrix notation as follows:

$$c = S^T diag(l) r + n_0 \quad , \tag{2.4.5}$$

where S^T denotes transposed matrix of camera channel characteristics; $diag(l)$ represents square matrix with illuminant power distribution values on the main diagonal; r is surface reflectance; n_0 denotes additive zero-mean Gaussian distribution noise. Additive noise is the noise from sensors, measurement errors of the spectral characteristics of sensors, illuminations and reflectances [25]. Additive noise is expressed as system noise and can be estimated using methods from [26]. Equation (2.4.5) defines relationships between camera response and true reflectance of the object under assumption of fixed illumination.

Figure 2.12 illustrates an example of reflectance samples spectra from different parts of the retinal spectral reflectance image. The curves represent similar behavior according to corresponding retinal location.

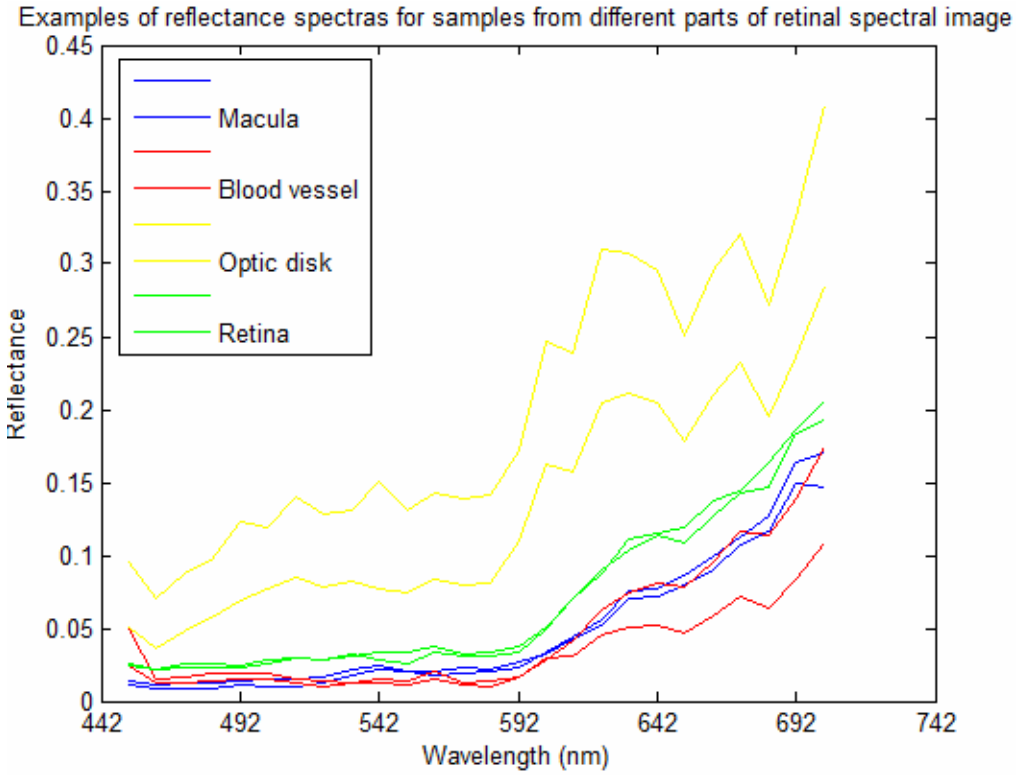

Figure 2.12. Spectral reflectances for retinal spectral image.

Chapter 3

SPECTRAL ESTIMATION AND APPROXIMATION

3.1 Introduction to Spectral Estimation

Medical applications and art-recovery are the fields, where the information from spectral imaging can provide significant benefits [1; 12; 17]. Due to high cost of the equipment, low speed of spectral image capture and claim of special skills in spectral measurement, these techniques are sometimes difficult to use. Conventional multichannel imaging is fast and easy to process, but it can not obtain accurate device and illuminant independent representation of the surfaces. Thus many researchers try to derive efficient method to estimate spectral image from multichannel measurements [14; 19; 20; 22; 24; 29].

Spectral estimation is a process of reflectance recovery using *a priori* knowledge about the characteristics of imaging device, noise properties and assumptions of reflectance properties. The usual way of estimation is to combine all the available knowledge in order to obtain estimation of the reflectance in some sampling grid. Spectral estimation often involves estimation of the spectral reflectance from the series of observations of the form as it was written in Equation (2.4.5). So the reflectance can be treated as an input signal under assumption of fixed illumination (l). All fixed parameters can be written jointly as in Equation (3.1.1):

$$F = diag(l)S\,, \tag{3.1.1}$$

and simplify the Equation (2.4.5) to a relationship Equation (3.1.2):

$$c = Fr + n_0 . \qquad (3.1.2)$$

Here F corresponds to multichannel sensor $F \in \Re^{k \times m}$, where $k<m$ and m are dimensions of the sampled reflectance. When the system function F is known, the estimation of reflectance r from system responses c is a linear inverse problem. Usually estimation techniques apply measured *a priori* data about the reflectance behavior [20; 29]. Some methods use low-spectral-dimensional and high-spatial-dimensional images of surface to be recovered and limited training set of the high-spectral-dimensional point-wise measurements of the same object [19; 24]. Other researchers try to capture color representation of the surface alternatively: by capturing several images of the surface under several illuminant conditions or by using additional filters in front of the multichannel camera [14; 24].

In some studies there is an assumption of reflectance distribution, which allows reflectance estimation to be done without any measured *a priori* information of reflectance data [22]. But it will not work if the assumption of the distribution is not correct enough.

This study is concentrated on those methods, which use only multichannel surface measurements and *a priori* data. The *a priori* data can be gathered from the training set of fundus reflectance images. It is important to remember that the quality of the training set based estimation often depends on the quality and size of the training set. Small number of spectral measurements or poor representation of the reflectance properties can strongly diminish the fidelity of the estimation. Further sections of the current chapter present three estimation methods and fidelity criteria for evaluation of the estimation.

3.2 Wiener Estimate

Wiener estimate (Least Mean Square Filter) [11] is one of the most adopted linear filters for the estimation of reflectance spectra. The aim of the estimation is to find

matrix W that can transform camera response c under assumption of Equation (3.1.2) into the estimated reflectance $\hat{r}$:

$$\hat{r} = Wc \tag{3.2.1}$$

with minimal mean square error [20]:

$$e = \left\langle \left\| r - \hat{r} \right\|^2 \right\rangle, \tag{3.2.2}$$

where r is a true reflectance of an object, $\langle\ \rangle$ is an averaging operator and $\|\ \|$ is 2-norm operator.

Following explanation is based on [18] and [20]. Assume Equation (3.1.2) where n is noise. From a stochastic view $\hat{r}$ can be calculated as a conditional mean of r given c:

$$\hat{r} = \int P(r \mid c) r dr, \tag{3.2.3}$$

where $P(r|c)$ is a conditional probability density of r given c. If r and n are independent Gaussian distributions, meaning $E[r] = E[n] = 0$, then:

$$P(r \mid c) \propto P_{Gaussian}(r) P_{Gaussian}(n), \tag{3.2.4}$$

where the Gaussian distributions are written as:

$$P_{Gaussian}(r) = C_r \exp(-\frac{1}{2} r^T \sum\nolimits_r{}^{-1} r), \tag{3.2.5}$$

$$P_{Gaussian}(n) = C_n \exp(-\frac{1}{2} n^T \sum\nolimits_n{}^{-1} n) \tag{3.2.6}$$

where C_r and C_n are normalization constants and $\sum_r$ and $\sum_n$ are covariance matrices of reflectance and noise respectively.

Using Equations (3.2.3) – (3.2.6) we have [18]:

$$P(r \mid c) = P_{Gaussian}(r \mid c) \propto \exp\left[-\frac{1}{2} (r - r^*)^T \sum{}^{*-1} (r - r^*) \right], \tag{3.2.7}$$

where:

$$r^* = \sum_r F^T (F \sum_r F^T + \sum_n)^{-1} c, \quad (3.2.8)$$

$$\sum^* = [I - \sum_r F^T (F \sum_r F^T + \sum_n)^{-1} F] \sum_r \quad (3.2.9)$$

Covariance matrices are defined as:

$$\sum_r = E\{(r - \bar{r})(r - \bar{r})^T\}, \quad (3.2.10)$$

where $E\{\bullet\}$ denotes the expected value operation and $\bar{r} = E\{r\}$ is the mean value of r. For the estimation of the reflectance, $\sum_r$ is usually calculated from all available samples of the training set.

Noise is commonly modeled as zero-mean Gaussian white noise process. In the current study the noises of the different channels are assumed to be identical and independent. Thus the correlation matrix for the noise is equal to:

$$\sum_n = s_n^2 I, \quad (3.2.11)$$

where s_n^2 is the noise energy for every of C spectral channels, and I denotes identity matrix, where all values are zeros except main diagonal with values equal to ones.

3.3 First-order Markov process

Another well-known linear estimate can be obtained using first-order Markov process (MP) [22]. In this case inverse operator is written as:

$$W_M = \sum_M F^T (F \sum_M F^T + \sum_n)^{-1}, \quad (3.3.1)$$

where the covariance matrix $\sum_M$ is estimated using a first-order Markov process covariance matrix of the form:

$$\sum_{M} = \frac{s_c^2}{Q}\begin{bmatrix} 1 & r & r^2 & . & . & r^{Q-1} \\ r & 1 & r & . & . & r^{Q-2} \\ . & & & & & . \\ . & & & & & . \\ r^{Q-1} & . & . & . & . & 1 \end{bmatrix}, \tag{3.3.2}$$

where s_c^2 represents energy of the reflectance and r is the adjacent element correlation factor in range [0,1].

One advantage of first-order Markov process based linear estimate is that it does not require any *a priori* knowledge about the true reflectance. Thus the method does not require a training set of spectral measurements.

3.4 Gaussian Mixture Model

Murakami et al. [20] proposed a Gaussian mixture distribution based nonlinear estimation method (GMM). GMM minimizes the mean square error of estimates under the assumption that the distribution of reflectance is a mixture of Gaussian sequences. Further description in current section is based on paper [20].

Probability density distribution of a sequence r as Gaussian mixture distribution can be written as:

$$P^M(r) = \sum_{k=1}^{K} w_k p_k(r), \tag{3.4.1}$$

where superscript M indicates a mixture distribution, K is the number of the components, w_k is the k^{th} weight coefficient in range [0,1], and $p_k(r)$ is the k^{th} component Gaussian density of the form:

$$p_k(r) = C_k \exp\left[-\frac{1}{2}(r - \langle r_k \rangle)^T \sum_k^{-1} (r - \langle r_k \rangle)\right], \tag{3.4.2}$$

where C_k is the normalization constant such that $\int P(r)dr = 1$, $\langle r_k \rangle$ is the mean of sequence r, and $\sum_k$ is the covariance matrix of r.

The conditional probability density of reflectance r given camera responses c is:

$$P(r \mid c) = AP^{M}(r)P^{G}(n), \tag{3.4.3}$$

where A is a normalization constant such that $\int P(r \mid c)dr = 1$, and $P^{G}(n)$ is Gaussian distribution of additive noise.

Substituting Equation (3.4.1) into Equation (3.4.3) gives:

$$P(r \mid c) = A\sum_{k=1}^{K} w_k p_k(r)P(n) \tag{3.4.4}$$

It can be written:

$$w_k p_k(r)P(n) = B_k p_k(r \mid c), \tag{3.4.5}$$

where $p_k(r \mid c)$ is the probability density of r given c when r is a random sequence of $p_k(r)$, and B_k is a proportion coefficient such that:

$$B_k = \int w_k p_k(r)P(n)dr. \tag{3.4.6}$$

Now the estimate of reflectance $\hat{r}$ can be calculated as the conditional mean of r given c as follows:

$$\hat{r} = \int P(r \mid c)rdr = A\sum_{k=1}^{K}[B_k \int p_k(r \mid c)rdr] = A\sum_{k=1}^{K} B_k \hat{r}_k, \tag{3.4.7}$$

where $\hat{r}_k$ is the best estimate of r if r is a random sequence of $p_{k(r)}$. Thus the estimate of reflectance $\hat{r}$ is the sum of weighted estimates $\hat{r}_k$.

In case of Gaussian mixture distribution every $p_{k(r)}$ is Gaussian like in Equation (3.4.2) and probability density of r given c becomes Gaussian as (see detailed derivation in [20]):

$$p_k(r \mid c) = \exp[-\frac{1}{2}(r - r_k^*)^T \sum\nolimits_k^{*-1} (r - r_k^*)], \tag{3.4.8}$$

where

$$r_k^* = \langle r_k \rangle + \sum\nolimits_k F^T (F \sum\nolimits_k F^T + \sum\nolimits_n)^{-1}(c - F \cdot \langle r_k \rangle) \tag{3.4.9}$$

and

$$\sum_k^* = [I - \sum_k F^T (F \sum_k F^T + \sum_n)] \sum_k \quad , \tag{3.4.10}$$

assuming mean vector $\langle r_k \rangle$ is not zero.

Estimate $\hat{r}_k$ corresponds to the Wiener estimate using *a priori* information from Gaussian distribution $p_k(r)$. Ensemble of training samples to formulate the K Gaussian densities can be divided into k sub portions, for example, by *c-Means* clustering. Coefficients B_k can be obtained from Equation (3.4.6) as follows:

$$w_k p_k(r) P(n) = w_k C_k C_n \exp[-\frac{1}{2} D_k] \exp[-\frac{1}{2} (r - r_k^*)^T \sum_k^{*-1} (r - r_k^*)], \tag{3.4.11}$$

where

$$C_k = \frac{1}{(\sqrt{2p \mid \sum_k \mid})^K}, \tag{3.4.12}$$

$$C_n = \frac{1}{(\sqrt{2p \mid \sum_n \mid})^K} \tag{3.4.13}$$

are normalization constants and:

$$D_k = (c - F \langle r_k \rangle)^T (F \sum_k F^T + \sum_n)^{-1} (c - F \langle r_k \rangle) . \tag{3.4.14}$$

From Equation (3.4.11) coefficients B_k can be calculated as follows:

$$\begin{aligned} B_k &= \int (w_k C_k C_n \exp[-\frac{1}{2} D_k] \exp[-\frac{1}{2} (r - r_k^*)^T \sum_k^{*-1} (r - r_k^*)]) dr \\ &= w_k C_k C_n \exp[-\frac{1}{2} D_k] \int \exp[-\frac{1}{2} (r - r_k^*)^T \sum_k^{*-1} (r - r_k^*)] dr \\ &= w_k C_k C_n \exp[-\frac{1}{2} D_k] \sqrt{(2p)^K \mid \sum_k^* \mid} \end{aligned} \quad . \tag{3.4.15}$$

Normalization constant A in Equation (3.4.3) is now calculated as:

$$A = \frac{1}{\sum_{k=1}^{K} B_k} . \tag{3.4.16}$$

The weight of mixing for each of estimate r_k^* will become:

$$m_k = \frac{B_k}{\sum_{j=1}^{K} B_j} \tag{3.4.17}$$

Finally the estimate of reflectance can be calculated as a linear combination of Wiener estimates r_k^*:

$$\hat{r} = \sum_{k=1}^{K} m_k r_k^*, \tag{3.4.18}$$

In order to preliminary classify training data and obtain k clusters $\hat{r}_k$, for $k = 1,..,K$, *c-Means* clustering algorithm was used. Following briefly presents steps of *c-Means* [30].

Algorithm 1: *c-Means.*

Choose arbitrary initial estimates of cluster representatives $q_j(0)$ for *j=1..K* (number of clusters).

Repeat:

For *i*=1 to N (total number of candidate elements)

Determine the closest representative q_j for candidate r_i.

Set indicator of residence to cluster $b_i=j$.

End For

For *j*=1 to K

Parameter updating: Determine q_j as the mean of the vectors r_i with $b_i=j$.

End For

Until no change in any of q_j occurs between two successive iterations.

The dissimilarity between vectors r_i and cluster representatives q_j is measured with square Euclidian distance as follows:

$$D(q,U)=\sum_{j=1}^{N}\sum_{j}^{K}u_{ij}\left\|r_i-q_j\right\|, \tag{3.4.19}$$

where $u_{ij}\in(0;1)$ is the membership coefficient indicating whether candidate r_i belongs to cluster j or not under constrain that it belongs to only one of the clusters:

$$\sum_{j=1}^{K}u_{ij}=1. \tag{3.4.20}$$

3.5 Error Metrics for the Evaluation of Estimation Accuracy

Current paragraph describes metrics used for evaluation of the estimation fidelity [11]. One of the well known objective fidelity criteria is the *root-mean-square-error* (*RMSE*). RMSE was used to express difference between measured and estimated spectral images. In the following description measured reflectance of the surface is denoted as $r_{i,j}$ and estimated reflectance at the same coordinates is $\hat{r}_{i,j}$.

The error between these two values is their difference. Then the overall error between two reflectance images is:

$$e=\sum_{i=1}^{N\cdot M}\sum_{j=1}^{C}(\hat{r}_{i,j}-r_{i,j}) \tag{3.5.1}$$

where N and M are spatial height and width of the reflectance image and C is the number of spectral dimensions of the image.

The *mean-square-error* (*MSE*) is the squared error average over the image as follows:

$$MSE=\frac{1}{N\cdot M\cdot C}\sum_{i=1}^{N\cdot M}\sum_{j=1}^{C}(\hat{r}_{i,j}-r_{i,j})^2 \tag{3.5.2}$$

Finally, *RMSE* is the square root of the squared error average over the image:

$$RMSE = \sqrt{\frac{1}{N \cdot M \cdot C} \sum_{i=1}^{N \cdot M} \sum_{j=1}^{C} (\hat{r}_{i,j} - r_{i,j})^2} \quad (3.5.3)$$

Another error metric is *peak signal-to-noise ratio* (*PSNR*):

$$PSNR = 10 \cdot \log_{10} \frac{\max_J^2}{MSE} \quad (3.5.4)$$

where $\max_J$ is the maximum of the j^{th} spectral channel of the image. In the experimental part of this study to evaluate image quality and to adjust additional Gaussian white noise PSNR was used.

3.6 Principal Component Analysis

Well known approximation method - Principal Component Analysis (PCA), which provides optimal estimation in terms of data variance, was used for the approximation of the spectral images in this study. PCA linearly transforms an original dataset into a set of uncorrelated variables – *principal components (PCs).* Based on the eigendecomposition of covariance matrix, PCA projects original dataset onto an ortonormal subspace of eigenvectors in a way, that the average of squared error is minimized and the data variance is maximized [8]. The PCA process is as follows [15; 16]:

1. Calculate the mean $\bar{r}$ of the distribution $\{r_i\}_{i=1}^{N}$ and subtract the mean value from each corresponding band;
2. Calculate the covariance matrix of the distribution $\{r_i\}_{i=1}^{N}$;
3. Find the eigenvalues $\{l_i\}_{i=1}^{M}$ of the covariance matrix and arrange them in decreasing order;
4. Choose the eigenvectors v_i, $i=1..k$ corresponding to largest eigenvalues;
5. Transform the initial data using eigenvectors $v_1..v_k$. Equation (3.6.1) represents the PCA approximation of the dataset, used in this study as an estimation benchmark:

$$\hat{r}_{PCA} = \sum_{i=1}^{k} v_i^T r v_i + \bar{r}, \qquad (3.6.1)$$

where i is an index of PC in the k-dimensional subspace, v_i is the i^{th} eigenvector of the covariance matrix.

Chapter 4

EXPERIMENT AND RESULTS

4.1 Dataset

In the current study 11 retinal spectral reflectance images of diabetic and non-diabetic human ocular fundi were used to investigate the performance of the estimation methods described in Chapter 3. Reflectance images were provided by the “InFotonics Center” research group, Joensuu. Images were obtained within the joint research project “ImageRet” by the University of Joensuu, the Lappeenranta University of Technology and the Kuopio University Hospital / University of Kuopio [10], funded by the Finnish Institute for Technology and Innovation.

Images were taken with modified ophthalmic fundus camera system based on Canon CR5-45NM fundus camera system (Canon, Inc.) and QImaging Retiga-4000RV digital monochrome CCD camera (QImaging Corp.) 1024×1024 pixels with 2×2 binning. Spectral radiance images were captured as monochrome digital images using transmittance filters in wavelength range from 400 to 694 nanometers with 10 nanometers sampling. The effect of illumination (illuminant D65 daylight) and the optics were corrected by dividing each spectrum in the spectral radiance image with a mean white reference spectrum (Spectralon ® diffuse non-fluorescent white reflectance sample) [10].

For each of the spectral reflectance images the borders of images were cut because the spectrum on the borders is too noisy and may increase estimation error. Two kinds of image fragments were used in this study: fragments of images without borders of size 925x875 (notated as IMGS2, IMGS3) and fragments of size

600x600 with optic disk and macula part (notated as IMGS2600, IMGS3600, IMGA600, IMGC600, IMG_S3600, IMGE600, IMGF600, IMGF2600, IMGG600, IMGH600, IMGM2600). The test set for all the estimation methods consists of fragments of images IMGS2, IMGS3 of size 925x875 and of size 600x600. Figure 4.1 presents RGB representation of spectral reflectance test images with detailed spectral parameters (beginning of the wavelength interval : sampling : end of the wavelength interval). The reflectance samples for the training set were taken from set of 600x600 fragments of spectral images IMGA600, IMGC600, IMG_S3600, IMGE600, IMGF600, IMGF2600, IMGG600, IMGH600, IMGM2600. Figure 4.2 presents RGB representation of the training images with detailed spectral characteristics.

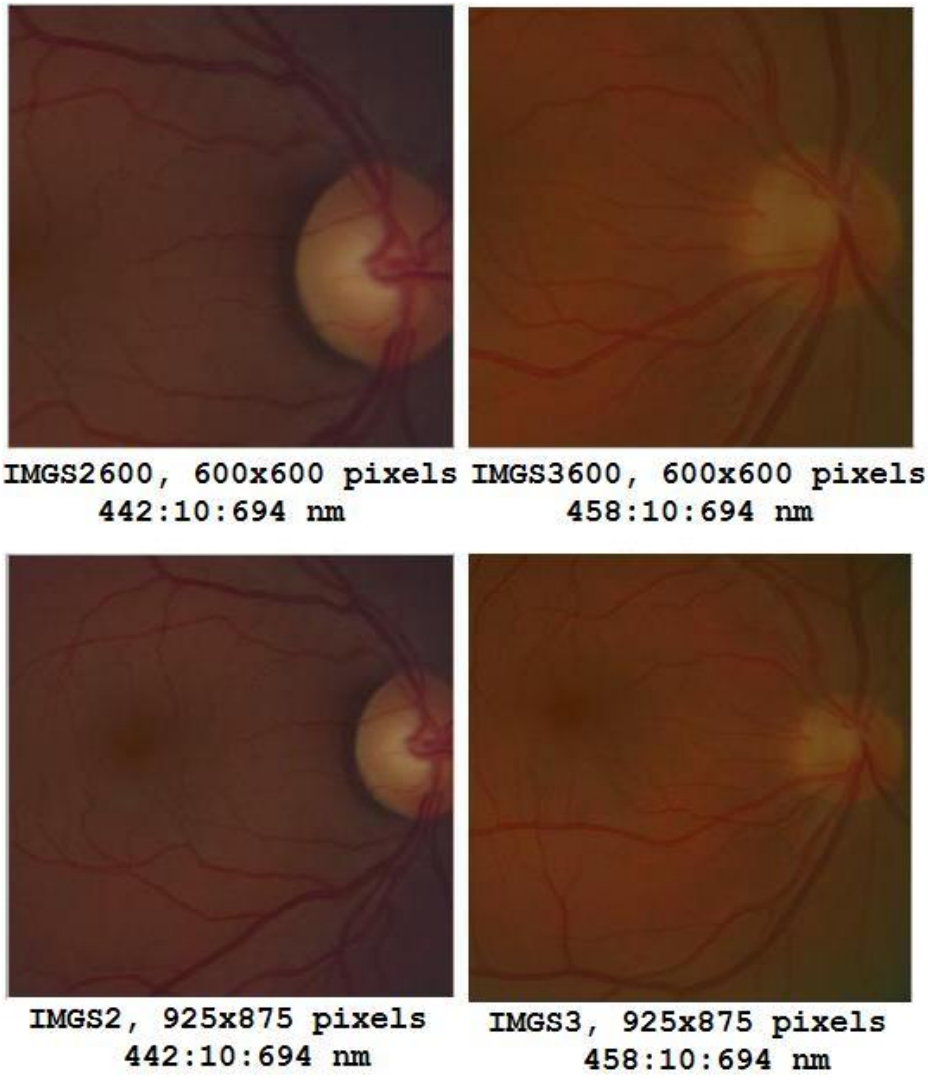

Figure 4.1. Frames of test images used in the study.

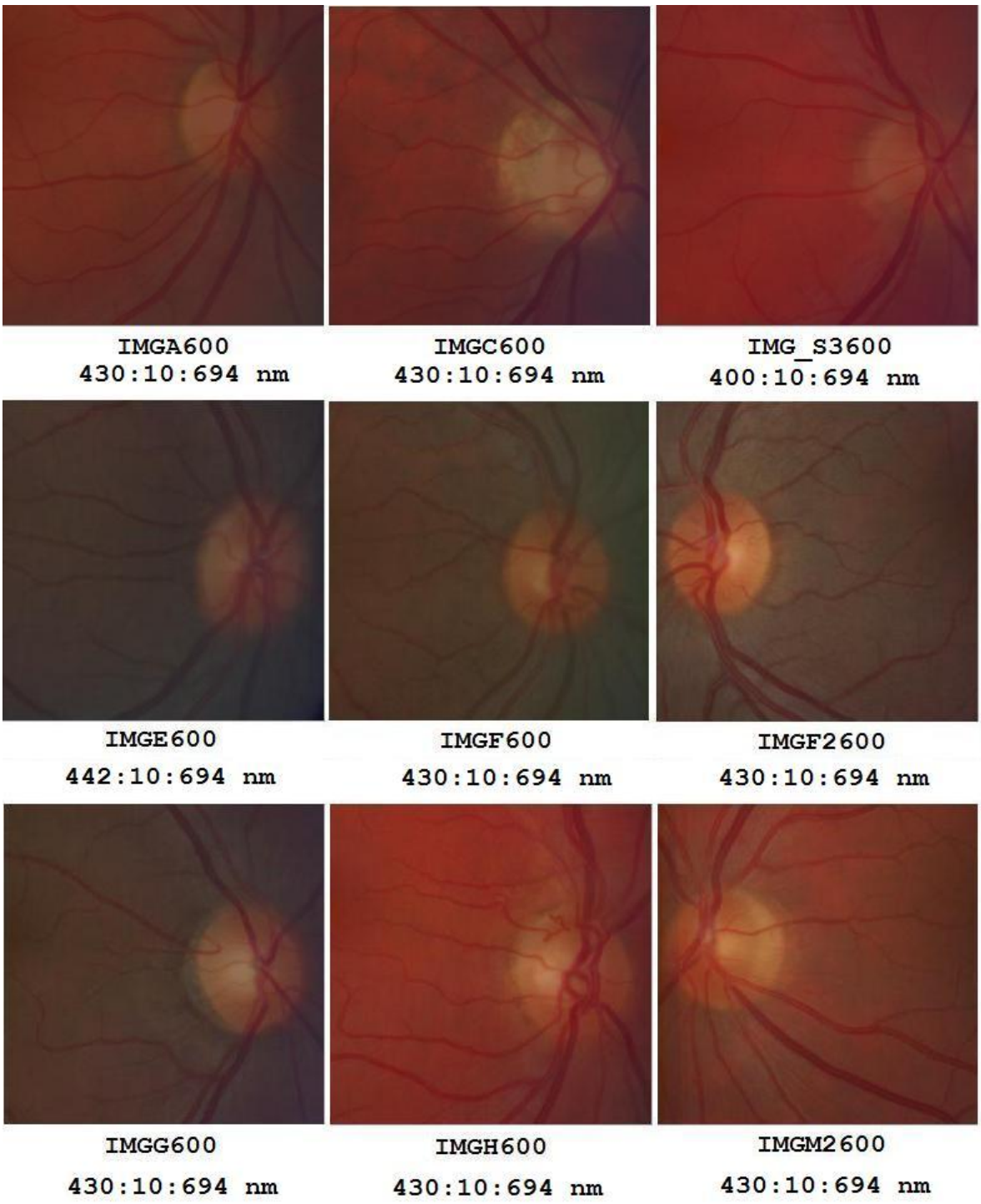

Figure 4.2. Training images used in the study.

Training sets for the test images were formed as follows. From each of the 9 test images 10000 samples of spectral reflectance (a regular grid 100x100) were chosen using wavelength range 442-694 nm and 10 nm sampling for the test images IMGS2 and IMGS2600, and in wavelength range 458-694 nm using 10 nm sampling for the test images IMGS3 and IMGS3600. Totally 90000 samples of spectrum vectors were obtained for both wavelength ranges. The RGB images of

retina for the test set were simulated according to Equation (2.4.5), using the reflectance images and the standard D65 “daylight” spectral power distribution as the illuminant.

Camera channel characteristics were modeled with the Gaussian functions:

$$s_i^{\,s}(l) = \frac{1}{2\sqrt{p \cdot s_i}} \exp\left[\frac{-(l - l_i)^2}{2 \cdot s^{\,2}_i}\right], \qquad (4.1.2)$$

where i indicates sensor and s_i^2 is the variance of the Gaussian. Figure 4.3 presents the shapes of the Gaussian sensitivities and additional transmittance filters used in the simulation. The purpose of using additional transmittance filters is to increase the amount of information in the measurements. In some studies it can be assumed that additional filters can be used in front of illuminant or camera. This method can be slow and needs additional work. Alternatively we can assume that the camera has eight channels. In the current study additional filters were used only in the estimation based on First-order Markov process (MP).

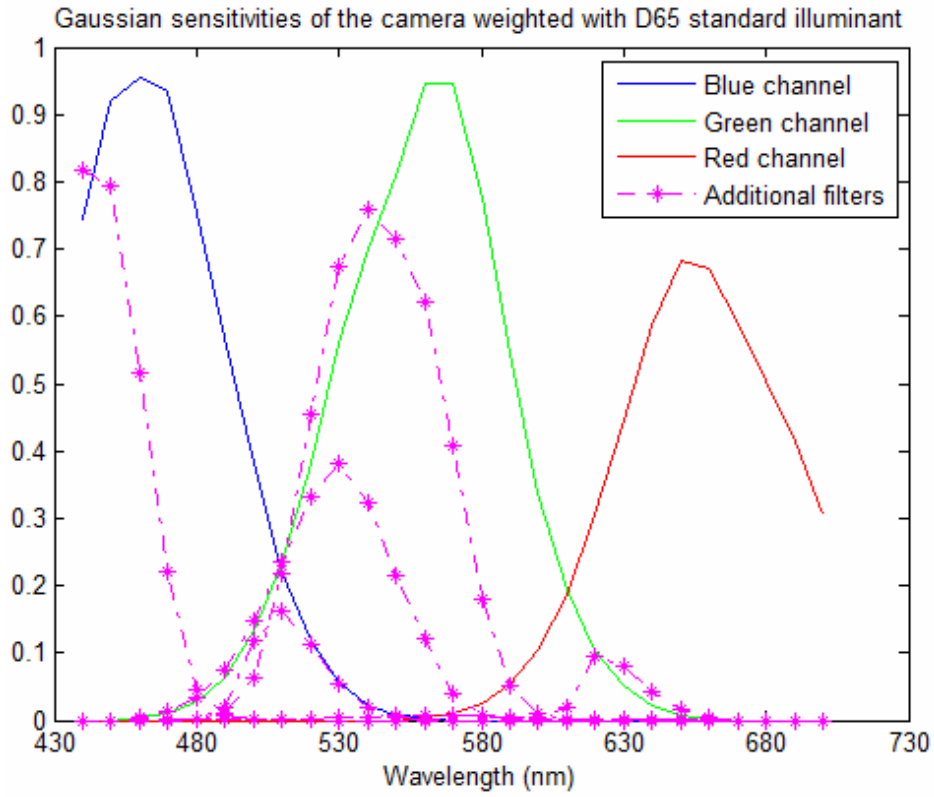

Figure 4.3. Eight camera sensitivities (3 Gaussian camera channels plus 5 additional transmittance filters) weighted with D65 standard illuminant.

Three levels of additional zero-mean Gaussian white noise with PSNR ∞ (no additional noise), 40dB and 30dB were used in the simulation. The performances of the estimations were evaluated with average value, standard deviation and maximal root-mean-square error between the estimated and the original retinal reflectance images.

4.2 Reflectance estimation using Wiener Estimate

Resulting RMSE values for the Wiener estimate are presented in Table 4.3. The estimate was also examined for the case, when the covariance matrix was formed of the reflectance samples from the test images respectively. Results are presented in Table 4.4.

Table 4.3. Errors of Wiener estimation for the test sets

Image		IMGS2	IMGS3	IMGS2600	IMGS3600
PSNR(dB)	RMSE				
∞	Avg.	0.0096	0.0107	0.0102	0.0103
	Max.	0.0473	0.0222	0.0476	0.0222
	Std.	0.0043	0.0027	0.0045	0.0028
40	Avg.	0.0104	0.0114	0.0110	0.0111
	Max.	0.0469	0.0255	0.0481	0.0266
	Std.	0.0042	0.0027	0.0043	0.0028
30	Avg.	0.0131	0.0151	0.0137	0.0146
	Max.	0.0466	0.0449	0.0487	0.0416
	Std.	0.0046	0.0039	0.0047	0.0039

Resulting error values for the estimation indicates that the estimation performance is good, since the average RMSE is less than 0.0107 for the noise-free images. Even under condition of high noise level the average RMSE value does not exceed 0.0151. Comparing by resulting error values it was found that the estimate with the

covariance matrix of reflectance samples from the test images does not perform better than the estimate with training set from the reflectance samples from the test images in noise-free case. It means that the reflectance spectra of retina seem to show similarity, so that the training set used for the estimation may represent general behavior of the retinal spectral reflectance shapes. It can also be seen from the results that maximum RMSE is higher than average RMSE. It means that some of spectrum estimations are very poor. In the additional noise cases it was found that the estimation does not perform much worse both in terms of average and maximum RMSE values.

Table 4.4. Errors of Wiener estimation for the test sets when the training set consist of the reflectance samples from the test set images respectively

Image		IMGS2	IMGS3	IMGS2600	IMGS3600
PSNR(dB)	RMSE				
∞	Avg.	0.0093	0.0106	0.0102	0.0103
	Max.	0.0473	0.0222	0.0473	0.0222
	Std.	0.0039	0.0028	0.0045	0.0028
40	Avg.	0.0102	0.0113	0.0110	0.0111
	Max.	0.0467	0.0258	0.0464	0.0291
	Std.	0.0038	0.0027	0.0043	0.0028
30	Avg.	0.0129	0.0151	0.0137	0.0146
	Max.	0.0478	0.0401	0.0476	0.0410
	Std.	0.0043	0.0039	0.0047	0.0039

4.3 Reflectance estimation using the first-order Markov process

Next, estimation of the reflectance with the first-order Markov process (MP) was examined. Since this estimate does not require any training set, only the simulated RGB images with different levels of additional Gaussian noise for the estimation

and reflectance images of the test set for the evaluation were used. Parameter r is usually taken to be from 0.9 [22] to 0.995 [19]. In this study r is taken to be 0.95.

Table 4.5. Errors of first-order Markov process estimation from 3 channel images

Image		IMGS2	IMGS3	IMGS2600	IMGS3600
PSNR(dB)	RMSE				
∞	Avg.	0.0169	0.0259	0.0175	0.0235
	Max.	0.0444	0.0459	0.0444	0.0413
	Std.	0.0041	0.0092	0.0047	0.0088
40	Avg.	0.0171	0.0257	0.0176	0.0235
	Max.	0.0445	0.0463	0.0442	0.0414
	Std.	0.0041	0.0091	0.0047	0.0087
30	Avg.	0.0185	0.0262	0.0190	0.0241
	Max.	0.0474	0.0483	0.0468	0.0439
	Std.	0.0042	0.0090	0.0048	0.0086

Table 4.6. Errors of first-order Markov process estimation for 8 channel input images (see channel characteristics on Figure 4.3)

Image		IMGS2	IMGS3	IMGS2600	IMGS3600
PSNR(dB)	RMSE				
∞	Avg.	0.0127	0.0163	0.0141	0.0163
	Max.	0.0359	0.0283	0.0359	0.0276
	Std.	0.0040	0.0052	0.0043	0.0052
40	Avg.	0.0146	0.0168	0.0158	0.0168
	Max.	0.0416	0.0317	0.0424	0.0298
	Std.	0.0041	0.0051	0.0043	0.0051
30	Avg.	0.0187	0.0195	0.0196	0.0195
	Max.	0.0560	0.0483	0.0544	0.0444
	Std.	0.0051	0.0054	0.0052	0.0053

Table 4.5 contains resulting error values of the estimation. The estimate performs almost two times worse when compared to the results for the Wiener estimate. Nevertheless the average RMSE value upper limit is 0.0259 for the noise-free images and 0.0262 for the noisy images. At the same time in terms of maximum RMSE MP performs well when compared to other methods. This result is good in respect that no *a priori* information of the reflectance distribution was used during the estimation.

For this method the multispectral images were also simulated as responses of the camera with 3 primary Gaussian sensitivities and 5 additional filters. Resulting RMSE values are presented in Table 4.6. It is obvious that the estimation works significantly better in case of using additional filters in about 0.01 better when compared to using only Gaussian sensitivities of camera. Even more, the estimation is about of same performance when compared to the Wiener estimate.

It was also discovered that MP performs almost twice better for the training images IMGS2 and IMGS2600 than for images IMGS3 and IMGS3600 in terms of average RMSE in case of not using additional filters. Use of additional filters provided decreasing of the difference in terms of average RMSE and decreasing of the maximum RMSE values for the test images IMGS3 and IMGS3600.

4.4 Reflectance estimation using Gaussian Mixture Model

For this method the test and training sets introduced in Section 4.1 were used. The clustering of the training set to 3 and 6 clusters using C-Means algorithm introduced in Section 3.5 was done as a preprocessing phase. The evaluation of the method for both clustering results is performed in Table 4.7 and Table 4.8. It was found that increasing the number of clusters does not improve estimation performance much. When this method was compared to Wiener estimate it was found that GMM improves the estimation performance up to 0.008 maximum. But

generally the performance of Wiener and GMM was concluded to be very similar. GMM performs better even for noised input images when compared to MP. It was also discovered that GMM performs worst in terms of maximum RMSE with respect to other methods.

Table 4.7. Errors of Gaussian Mixture Model estimation. 3 clusters

Image		IMGS2	IMGS3	IMGS2600	IMGS3600
PSNR(dB)	RMSE				
∞	Avg.	0.0104	0.0098	0.0095	0.0093
	Max.	0.0667	0.0239	0.0667	0.0239
	Std.	0.0052	0.0024	0.0047	0.0027
40	Avg.	0.0102	0.0106	0.0110	0.0102
	Max.	0.0733	0.0293	0.0716	0.0301
	Std.	0.0048	0.0024	0.0054	0.0027
30	Avg.	0.0129	0.0145	0.0137	0.0140
	Max.	0.0846	0.0445	0.0874	0.0457
	Std.	0.0057	0.0040	0.0068	0.0041

Table 4.8. Errors of Gaussian Mixture Model estimation. 6 clusters

Image		IMGS2	IMGS3	IMGS2600	IMGS3600
PSNR(dB)	RMSE				
∞	Avg.	0.0095	0.0109	0.0107	0.0102
	Max.	0.0845	0.0273	0.0845	0.0273
	Std.	0.0063	0.0030	0.0079	0.0026
40	Avg.	0.0103	0.0114	0.0114	0.0109
	Max.	0.0855	0.0309	0.0862	0.0304
	Std.	0.0063	0.0027	0.0079	0.0026
30	Avg.	0.0141	0.0152	0.0132	0.0147
	Max.	0.0921	0.0467	0.0898	0.0472
	Std.	0.0080	0.0041	0.0064	0.0042

4.5 Results and Discussion

According to the evaluation of the estimations with RMSE values, the Wiener method gives almost always the best performance for the noise-free images. The Tables 4.3, 4.7 and 4.8 also indicates the similarity of the performance quality when Wiener and GMM results are compared. Since GMM is a combination of several linear estimates, demanding some additional time for clustering and accurate adaptation to the training set distribution, it is more complex for modeling and calculations. Nevertheless, according to evaluation with RMSE criteria the model does not improve performance of the estimation for the used data.

MP shows relatively poor results of estimation when compared to Wiener and GMM, but the performance of the estimate may be acceptable for some applications. For highly noised input data the average RMSE value is double as much than the minimal among all estimates average RMSE, equal to 0.0129. Nevertheless the maximum RMSE value for the estimations is never higher than 0.0483 in the worst case (30dB PSNR noised image).

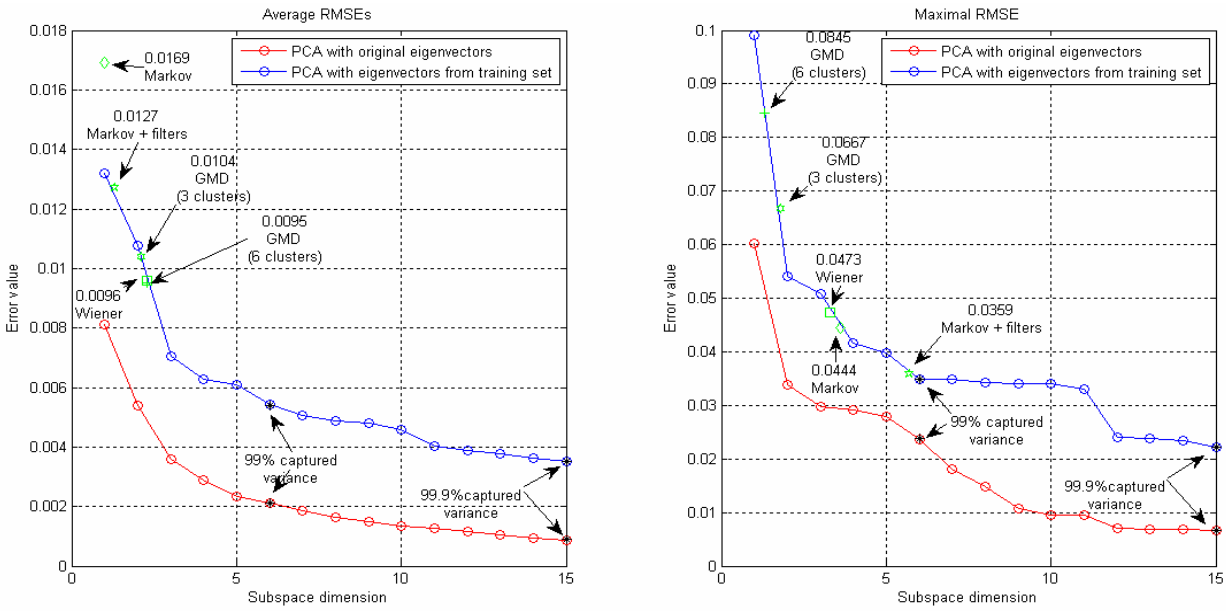

Figure 4.4. RMSE values for PCA approximation of the image IMGS2.

PCA approximations of the original test images were calculated to evaluate the quality of the estimates, where the most significant eigenvectors of the covariance matrices were used. Figures 4.4 – 4.7 show the RMSE values for the

approximation of the images using different subspace dimension. Corresponding numerical results of the evaluation can be found in Appendix 1 and Appendix 2. The graphs of RMSE value dynamics and table of results indicate that generally more than 3 principal components provide approximation with the maximal RMSE value less than 0.03 and fidelity more than 0.99. Also more then 11 principal components provide approximation with the captured 99.9% of variance. Thus none of the estimates can perform as good as the PCA approximation does.

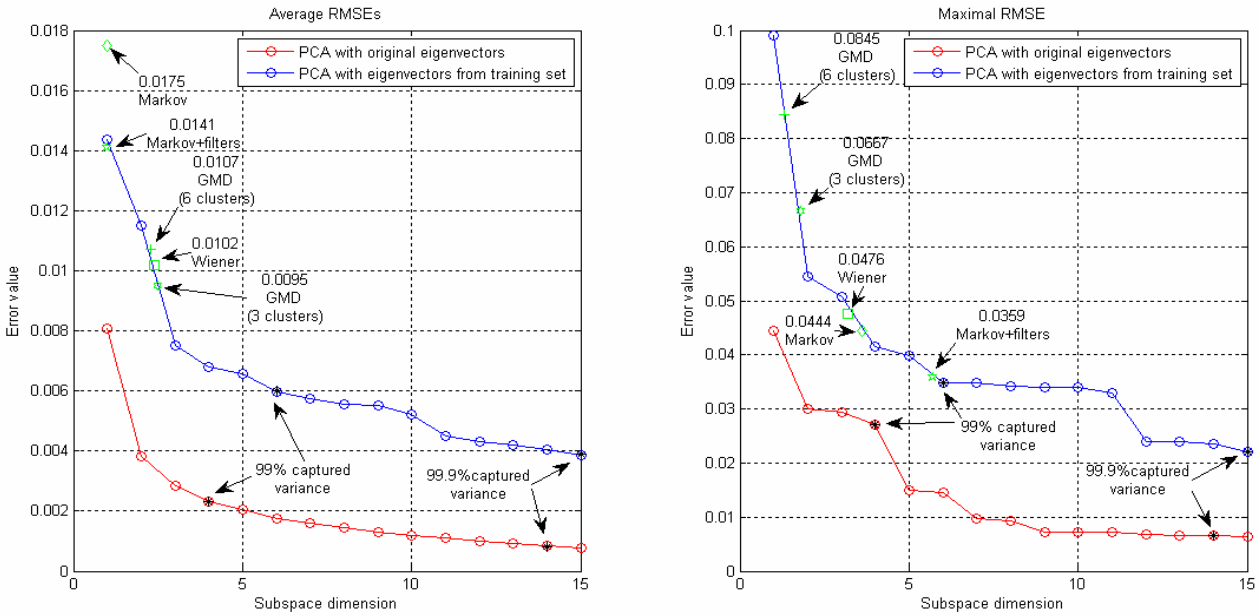

Figure 4.5. RMSE values for PCA approximation of the image IMGS2600.

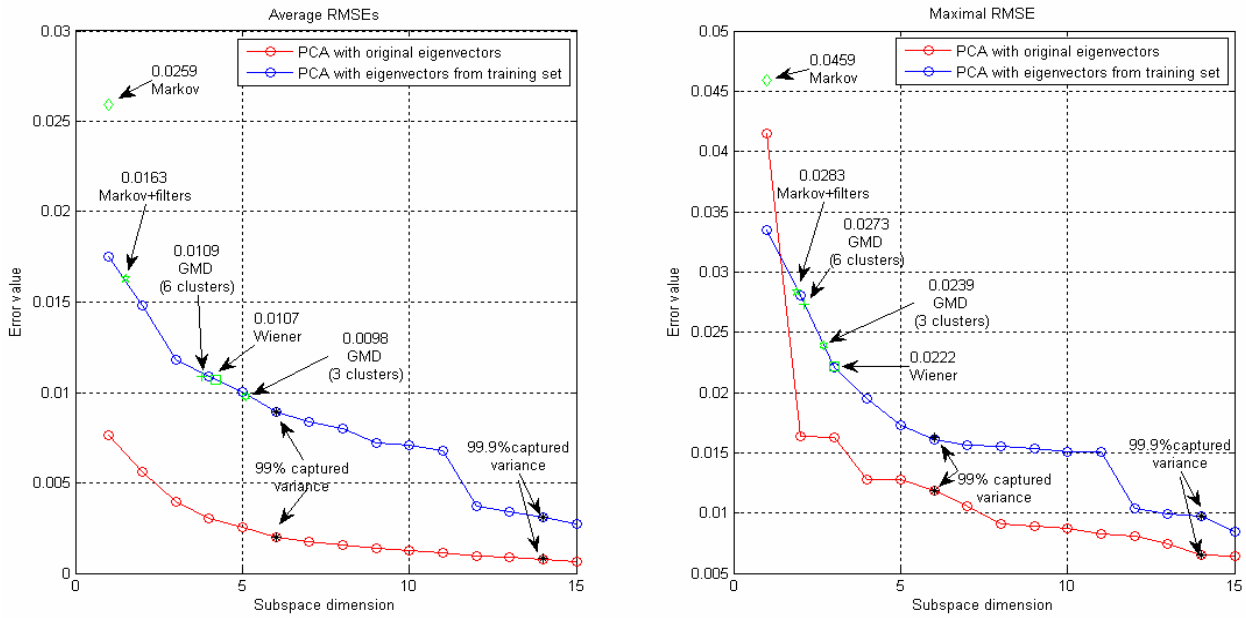

Figure 4.6. RMSE values for PCA approximation of the image IMGS3.

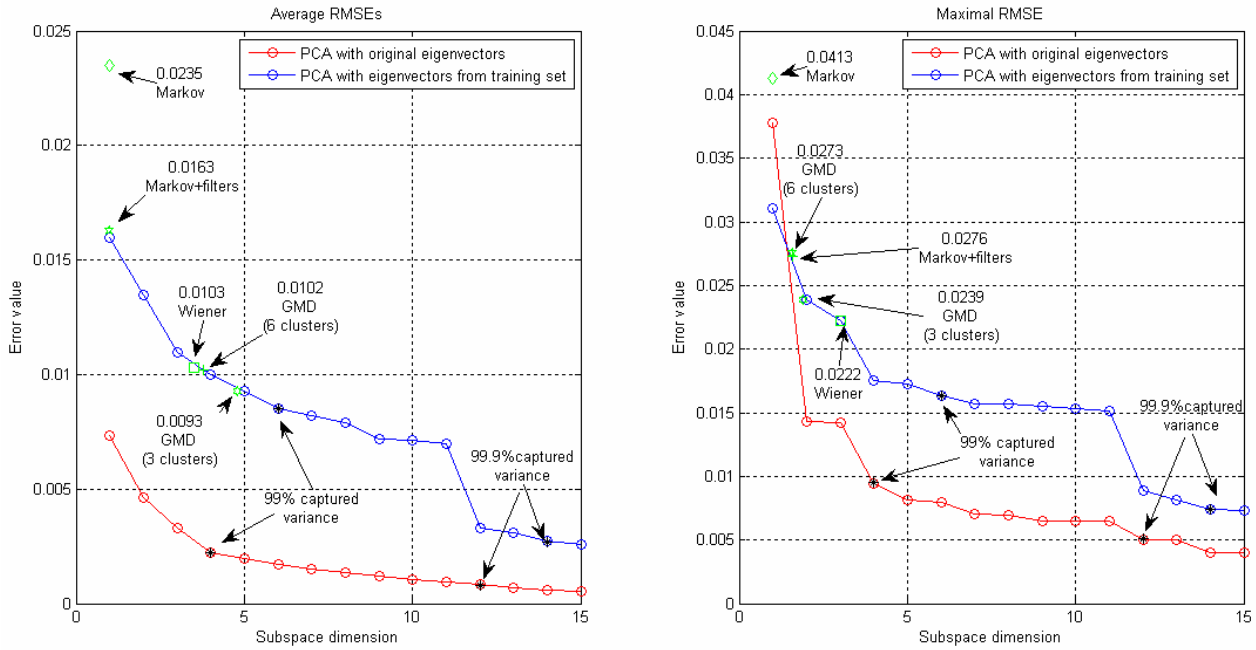

Figure 4.7. RMSE values for PCA approximation of the image IMGS3600.

Comparison of the estimation results indicates that the Wiener and GMM perform almost as good as the PCA approximation does with respect to the fact that PCA results correspond to ideal noise-free case. It is expected that the eigenvectors obtained from the training set are reasonable candidates for the camera channel functions when compare to the Gaussian function. This would provide better quality of the estimation.

Spatial distribution of the RMSE values for the estimations was examined. It should be noted that in the following Figures 4.8 – 4.12 the color scales of the RMSE values are different for the estimates and the comparison of the RMSE value levels of estimates should be done with respect to that fact. The analysis of the contours showed that commonly for all three examined estimates high estimation errors occur on the borders of the image, on the optic disk part and on the macula part of image. There may be lack of reflectance behavior representatives for optic disk and macula part, since the training samples of reflectance were taken from point-wise measured training images using regular spatial grid. The borders of the reflectance images also contain larger amount of noise when compared to other regions in the images. Thus it is expected that more

careful analysis of the training data and adaptive collection of the training samples can improve the estimation quality in these areas.

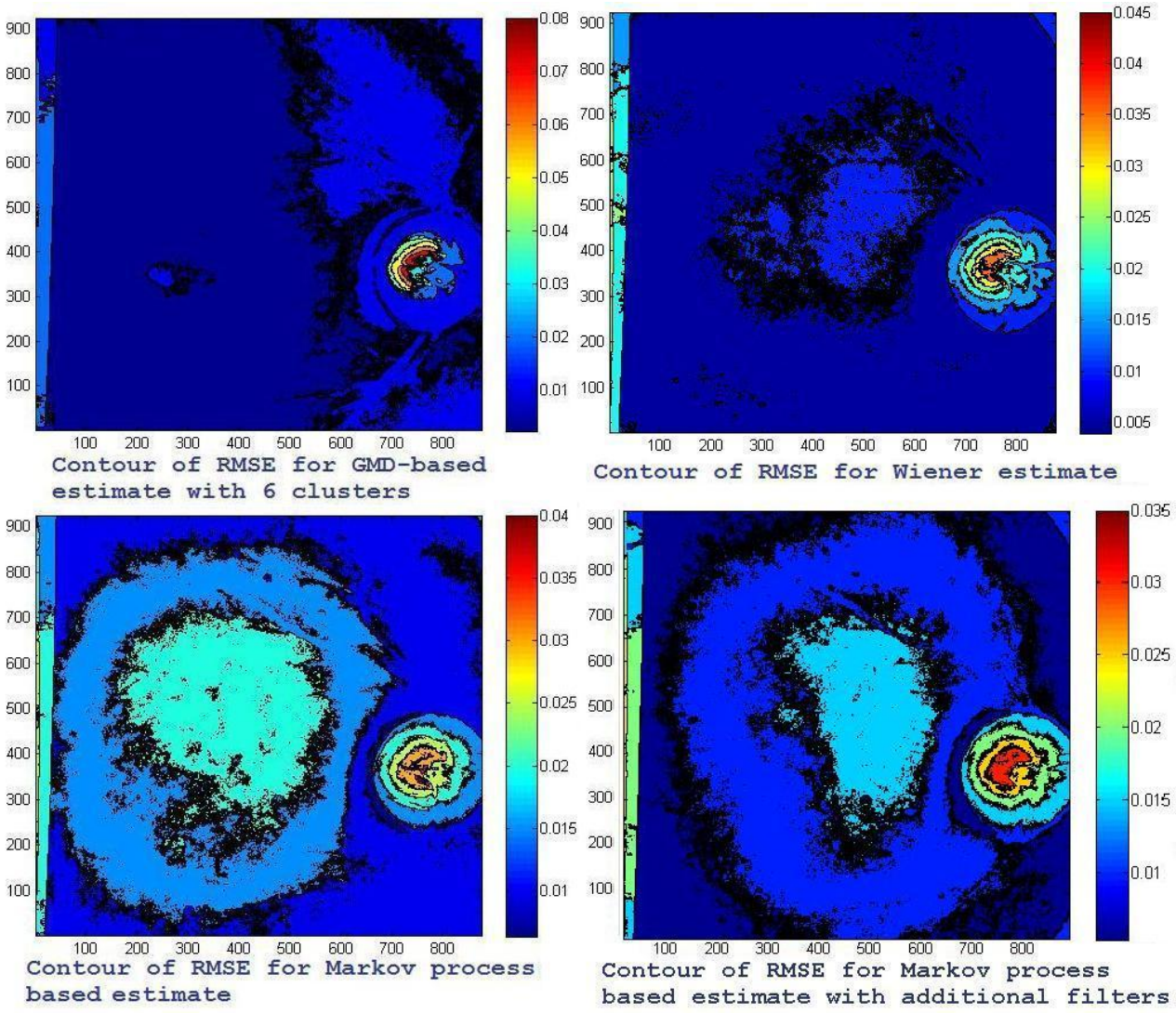

Figure 4.8. Color contours of the RMSE values for the image IMGS2 estimates.

Color contours of the RMSE values for the estimations of image IMGS2 are presented on Figure 4.8. For the Wiener estimate the Figure 4.8 indicates compact distribution of the high RMSE values: on the border, in the macula part of the image (central part of the retina) and on the optic disk part. For the MP the RMSE value distributed more smoothly with respect to same locations as for Wiener estimate. In case of the GMM the highest RMSE values are located in the brightest part of the optic disk part. Same comparison and the same results were obtained for

the estimations from the noised images with PSNR value equal to 30dB – highly noised images (Figure 4.9).

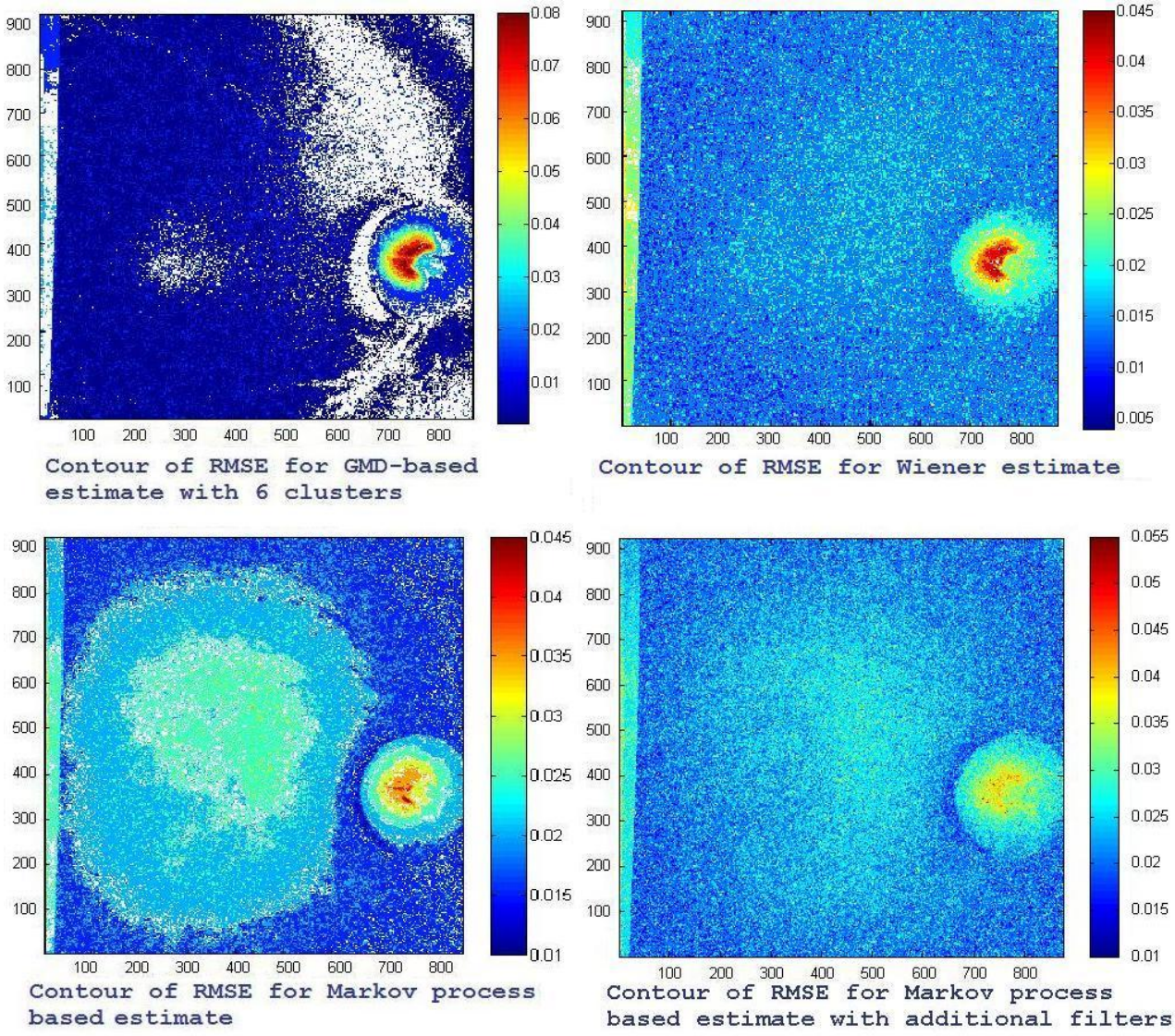

Figure 4.9. Color contours of the RMSE values for the image IMGS2 estimates under noise level of PSNR=30dB.

Some of the previous fundus studies [2; 32] concentrate their analysis to wavelength range from 390 to 540 nanometers. In this study the RMSE values of the estimations were examined in 3 intervals of wavelengths: from 400 to 500, from 500 to 600 and from 600 to 700 nanometers. The resulting contours of the RMSE distribution are presented in Figures 4.10 – 4.12. The Figure 4.10 indicates that in the wavelength range from 400 to 500 nanometers the GMM leads to RMSE values with upper limit equal to 0.025 in the optic disk part, and 0.013 for

the blood vessels and less than 0.01 in the macula part. Wiener estimate gives about the same performance with upper limit equal to 0.03 in the optic disk part, 0.013 for the blood vessels and less than 0.01 for the macula part. MP performs best when additional filters are used. The upper limit of RMSE value is 0.022 in the optic disk part, 0.01 for the blood vessels and 0.004 for the macula part. MP performed worse when only three Gaussian camera sensitivities were used in the estimation. The upper limit of RMSE value is 0.035 in the optic disk, 0.013 for the vessels and about 0.01 in the macula.

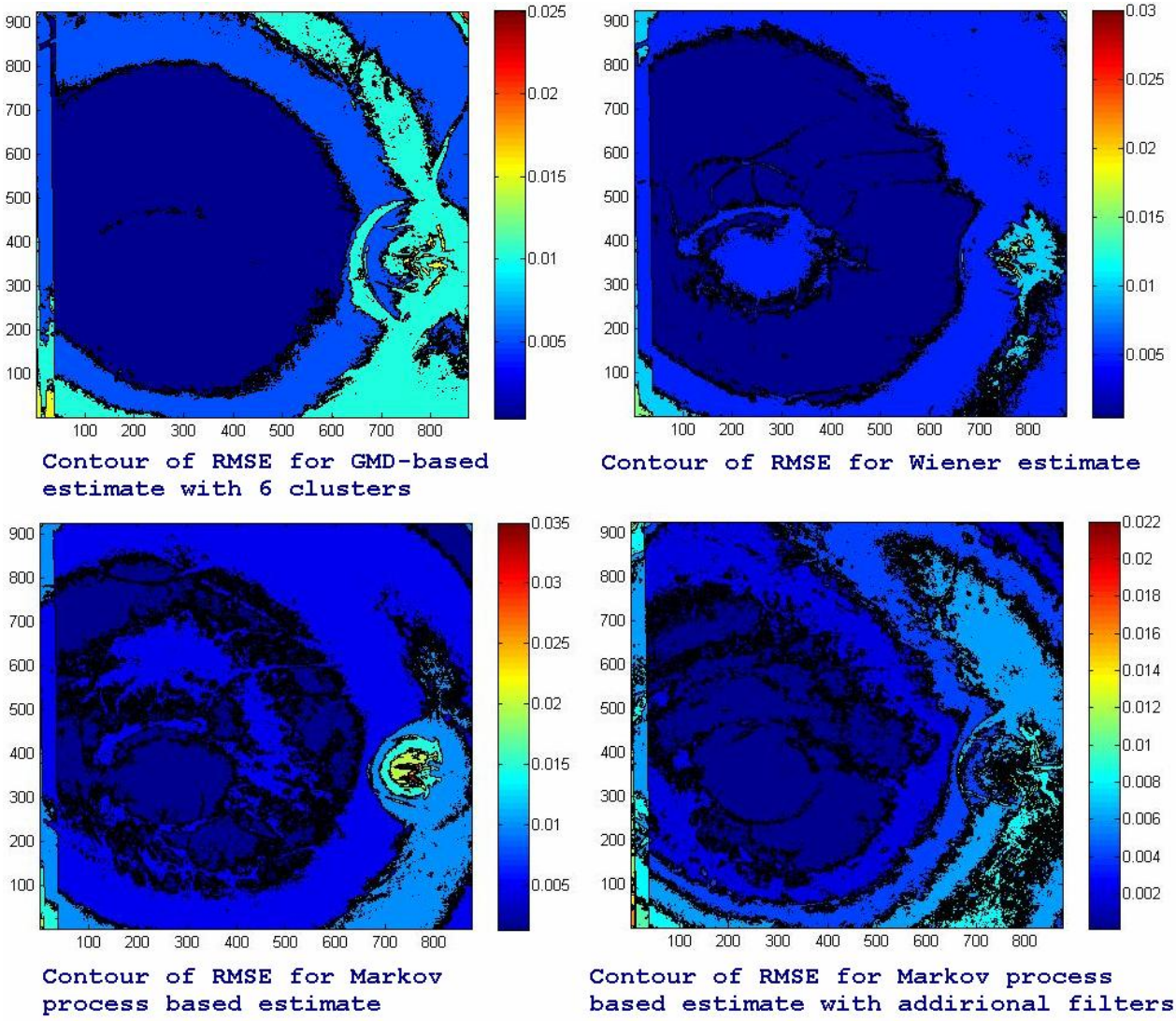

Figure 4.10. Color contours of the RMSE values for the image IMGS2 estimates in the wavelength range 400 to 500 nanometers.

In the wavelength range from 500 to 600 nanometers (Figure 4.11) GMM gives good performance with RMSE values less than 0.015 except the optic disk part,

where RMSE values can reach 0.06. The Wiener estimate gives better results: the upper limit of RMSE value is 0.055 in the optic disk part and less than 0.01 for other fundus parts. MP with only Gaussian camera sensitivities gives about the same performance: upper limit for the RMSE values in the optic disk part is 0.05, for the blood vessels is 0.01 and 0.02 for the macula part of the fundus. MP with additional filters gave the best performance for this wavelength range: the upper limit for RMSE values is 0.023 for the optic disk, 0.009 for the blood vessels and less than 0.005 for the macula part of the fundus.

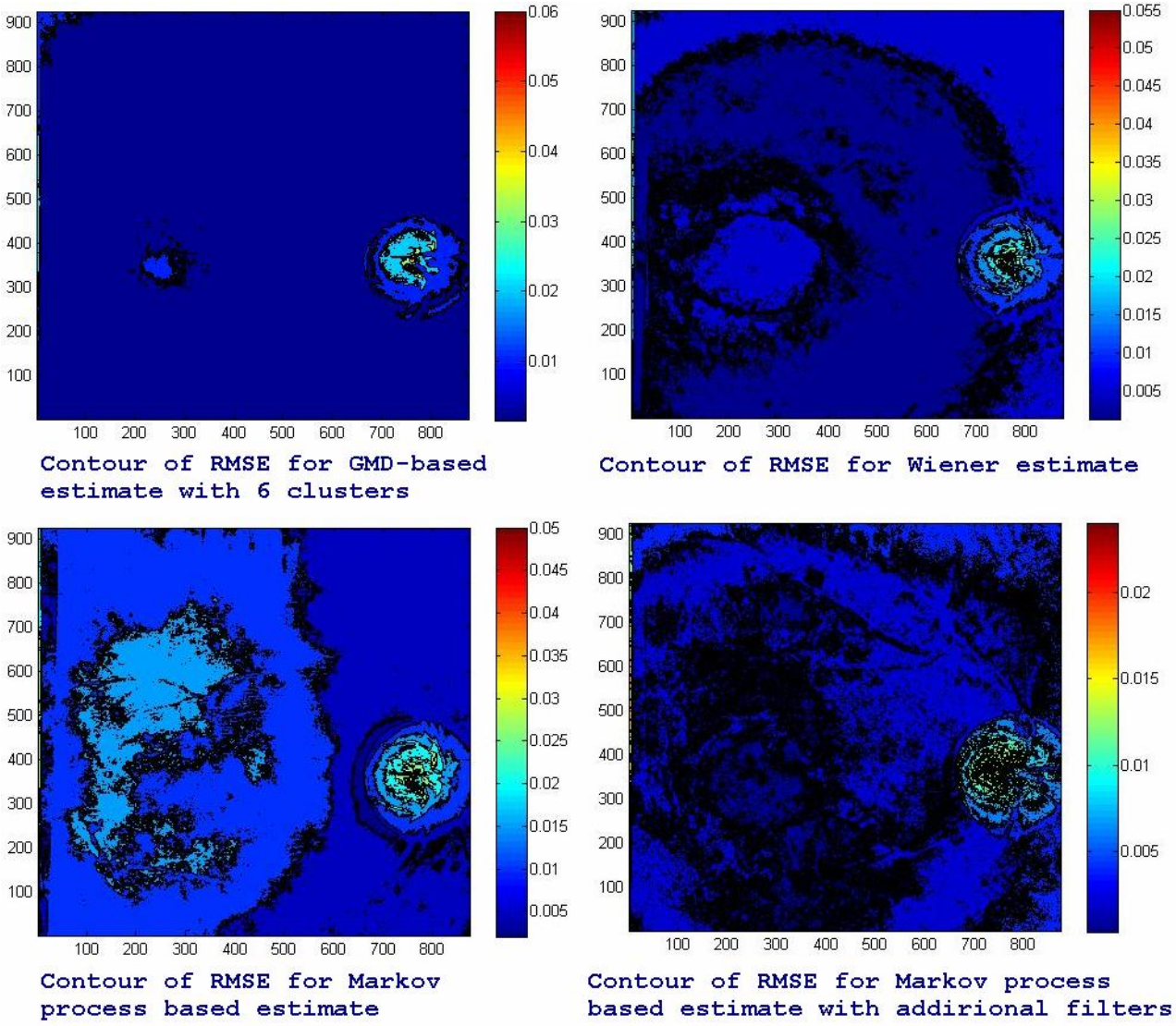

Figure 4.11. Color contours of the RMSE values for the image IMGS2 estimates in the wavelength range 500 to 600 nanometers.

In the wavelength range from 600 to 700 nanometers (Figure 4.12) Wiener estimate performs best among the studied estimates and has upper limit for the

RMSE values in the optic disk part to be 0.06, 0.02 for the blood vessels and 0.025 in the macular part of the fundus. GMM may give very high RMSE error in the optic disk part – up to 0.14 – at the same time the estimation error for the other parts of fundus image does not exceed the RMSE value of 0.02. MP in this investigation gave average performance both for 3 and 8 number of camera channels. For the MP with only Gaussian camera sensitivities the upper limit for the RMSE values in the optic disk part is 0.05, 0.025 for the blood vessels and 0.045 for the macula. For the MP with additional filters the upper limit for RMSE values is 0.06 in the optic disk, 0.025 for the blood vessels and 0.04 in the macula.

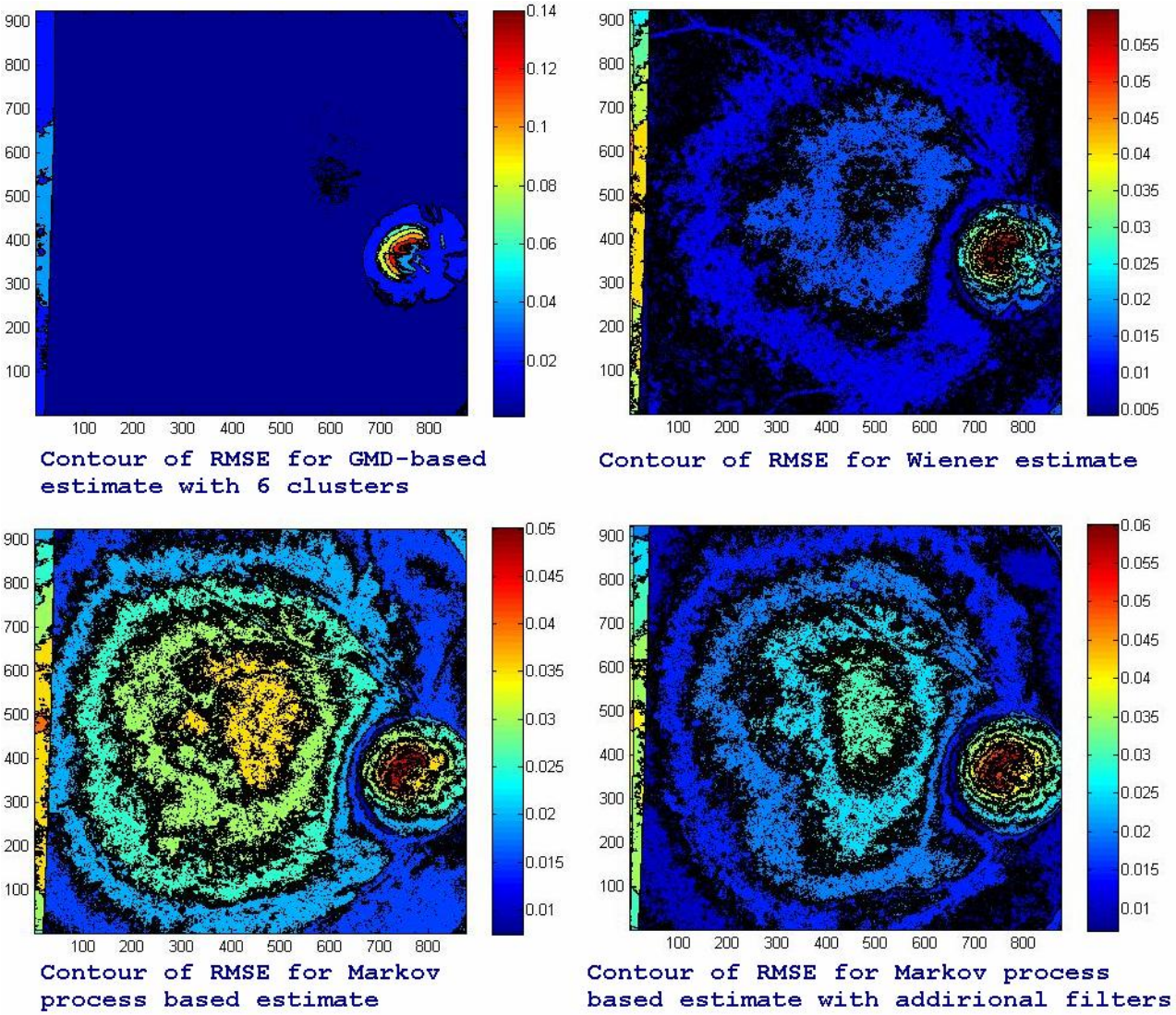

Figure 4.12. Color contours of the RMSE values for the image IMGS2 estimates in the wavelength range 600 to 700 nanometers.

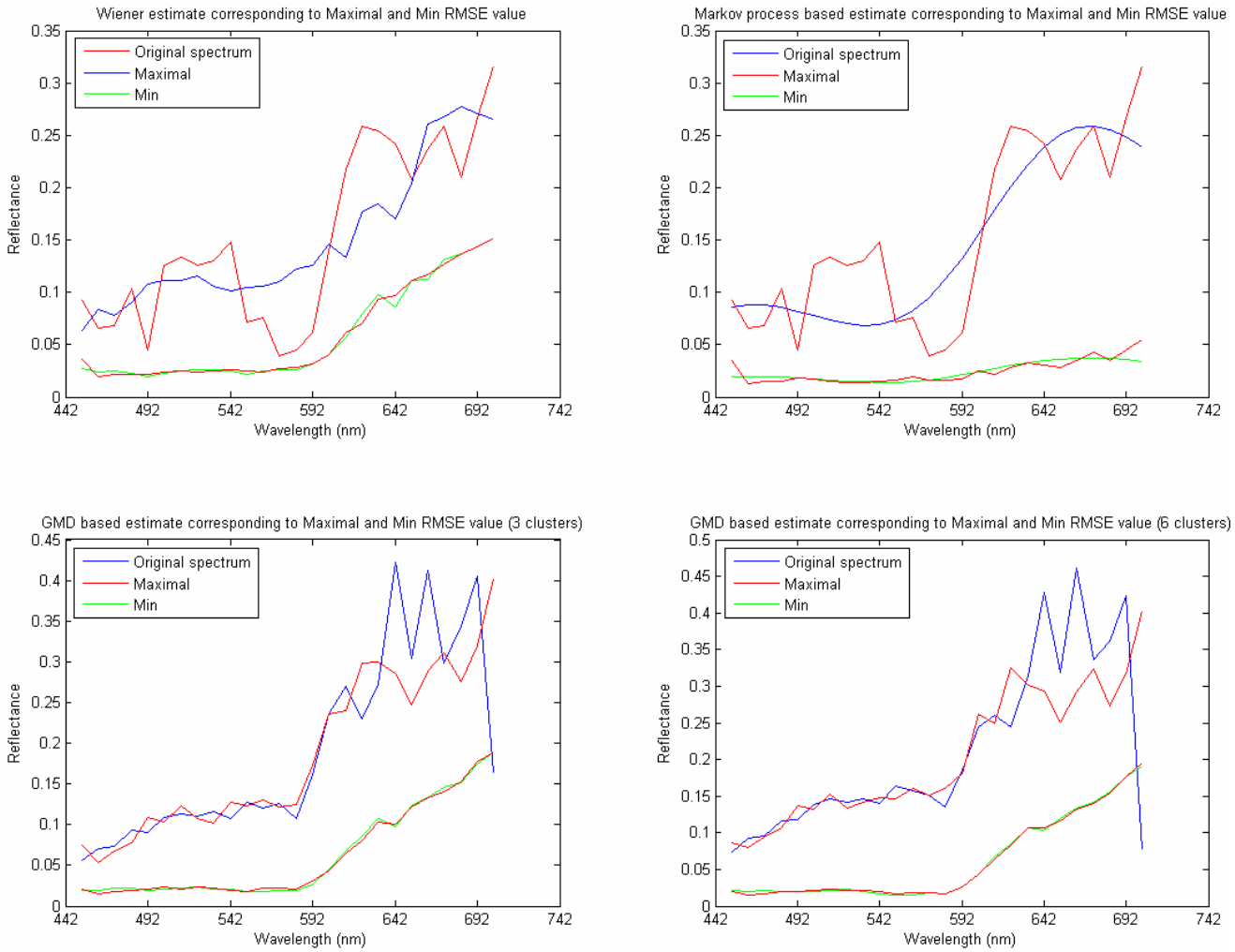

Figure 4.13. Spectra samples of best and worst estimation.

Comparisons of the best and the worst samples of estimations for the test image IMGS2 are presented in Figure 4.13. The Figure illustrates typical behavior of the MP – smooth and uniform shape of estimated reflectances – when other estimates attempt to follow the behavior of the reflectance. It can also be seen from the Figure 3.14 that there is probably varying amount of noise in the original measurements of reflectance images. In the real case this noise should be removed from the *a priori* reflectance data in order to guarantee reasonable estimation with respect to the true reflectance. General performance of the estimated spectral reflectance was also investigated when different spatial locations of fundus image are considered. Comparative graphs are presented in Figure 4.14.

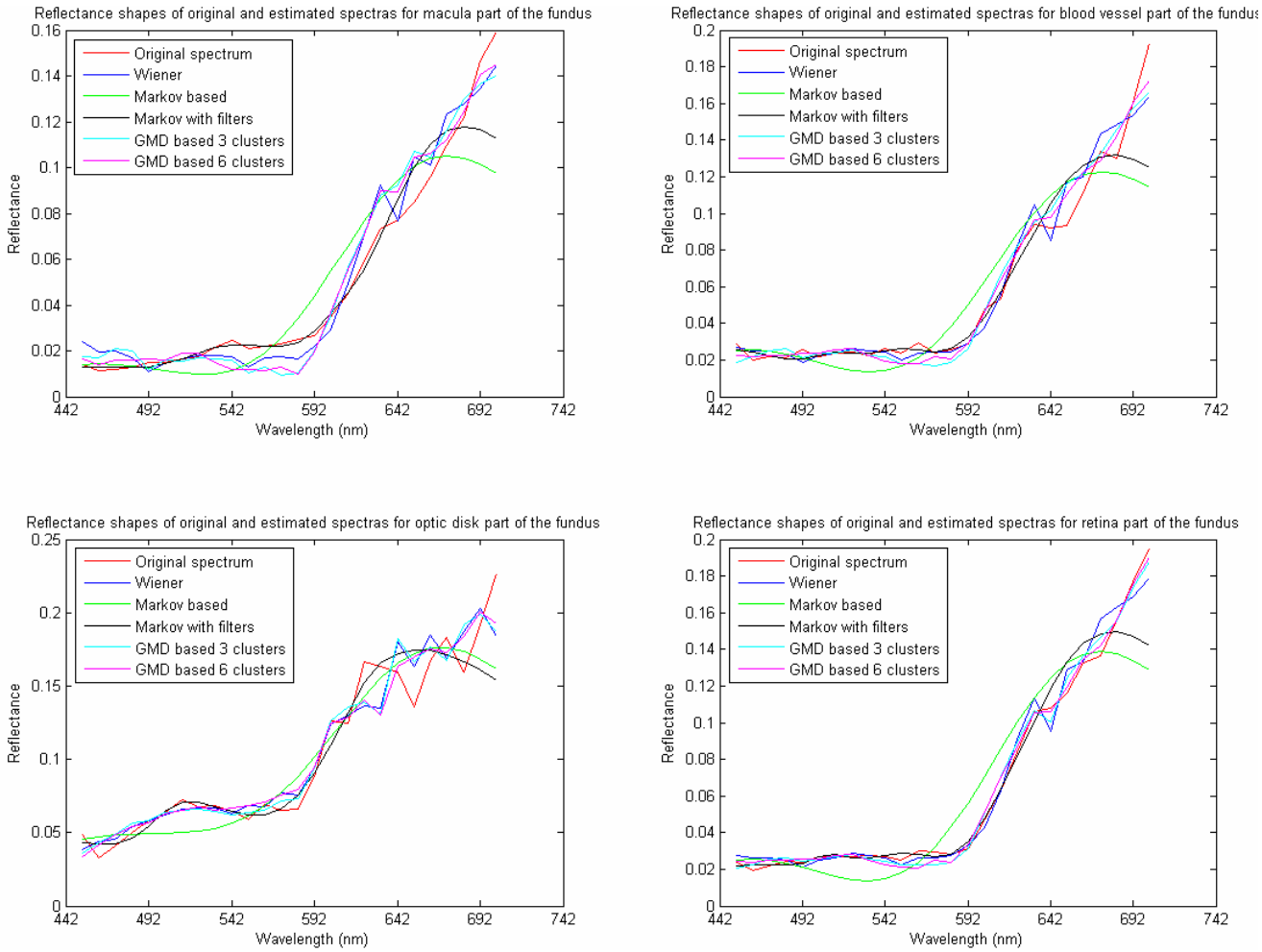

Figure 4.14. Spectral estimation samples from different parts of fundus image.

The examples of reflectance from different spatial locations show the same behavior, which was already discovered in the analysis of the RMSE contours. Additionally, despite the low maximum RMSE values, MP generally provides poor modeling of the spectral reflectance shape in all investigated cases.

Chapter 5

CONCLUSION

The aim of this work was to examine and compare some methods for the spectral reflectance estimation for fundus images. The key point of the study was the estimation of the spectral reflectance images from multichannel images. All the methods are point-wise and can be derived using the probabilistic framework, where the modeling of measurement noise is included. During the research Wiener, first-order Markov process (MP) and Gaussian Mixture Model (GMM) estimates were applied and their performance was compared. Although in general none of the estimates performs as good as the PCA approximation of the original spectral reflectance images, spatial investigation of the estimations identified that the Wiener estimate usually provides good fit of the estimation for the fundus, except optic disk part. It was discovered that linear Wiener estimate performs almost equally well with the nonlinear GMM estimate. It means that the data can be modeled using Gaussian distribution. Alternatively it was proposed to use Markov process based linear estimate, which does not depend on any *a priori* information about the retinal reflectance spectral distribution. MP uses only assumption for the reflectance distribution, illuminant and camera characteristics. The performance of this method is worse when compared to the other two methods, but still MP can give adequate performance for some applications. It was also discovered that MP, in case of reconstruction from 8-channel multichannel image, lead to comparable

performance with the Wiener estimation, based on three channel measurements. In practical imaging this method should be used only with digital camera with more than 3 channels. The results and simulated settings, presented in this study, should be validated with real multichannel measurements. It is expected that this research provides information for fundus image analysis. In the most optimistic case the studied methods lead to relatively fast and cheap way of obtaining retinal spectral reflectance images to further processing. It would also lead to practical way of storing the reflectance information.

It was discovered that the noise in the used reflectance data was not spatially uniform. In the further research it would be also useful to adjust the training sets according to spatial locations of the fundus. It is expected that using modified training set would lead to better estimation results. When the results are analyzed it can be suggested, that more careful investigation of data, collection of the training set, and improvement of the clustering method would improve the performance of the estimation.

BIBLIOGRAPHY

[1] T.T.J.M. Berendschot, P.J. DeLint, D. van Norren: “Fundus reflectance – historical and present ideas”, Progress in Retinal and Eye Research 22, 171-200 (2003).

[2] T.T.J.M. Berendschot, D. van Norren: “Objective determination of the macular pigment optical density using fundus reflectance spectroscopy”, Archives of Biochemistry and Biophysics 430, 149-155 (2004), available online at www.sciencedirect.com.

[3] R. Bracewell, "The Impulse Symbol", New York: McGraw-Hill, 2000.

[4] B. Cassin, S. Solomon: *Dictionary of Eye Terminology,* Gainsville, Florida, Triad Publishing Company, 1990.

[5] V. Cheung, S. Westland: “Characterization of trichromatic color cameras by using a new multispectral imaging technique”, J. Opt. Soc. Am. A 7, 1231-1240 (2005).

[6] D. Connah, J. Y. Hardeberg: “Spectral recovery using polynomial models”, SPIE vol. 5667, 65-75 (2005).

[7] J. M. DiCarlo, B. A. Wandell: “Spectral estimation theory: beyond linear but before Bayesian”, J. Opt. Soc. Am. A 7, 1261-1270 (2003).

[8] R.O. Duda, P.E. Hart, D.G. Stork: *Pattern Classification*, 2nd Edition, John Wiley & Sons, Inc., 2001.

[9] B. Fraser, C. Murphy, F. Bunting: *Real World Color Management: Industrial Strength Production Techniques*, 2003.

[10] P. Fält, J. Hiltunen, M. Hauta-Kasari, I. Sorri, V. Kalesnykiene, and H. Uusitalo: "Extending Diabetic Retinopathy Imaging from Color to Spectra", 16th Scandinavian Conference on Image Analysis (SCIA 2009), June 15-18, 2009, Oslo, Norway.

[11] R. Gonzalez, R. Woods: *Digital Image Processing,* Addison-Wesley, 1992.

[12] H. Haneshi, T. Hasegawa, A. Hosoi, Y. Yokoyama, N. Tsumura, Y. Miyake: "System design for accurately estimating the spectral reflectance of art paintings", Appl. Opt. 35, 6621-6632 (2000).

[13] V. Heikkinen, T. Jetsu, J. Parkkinen, M. Hauta-Kasari, T. Jaaskelainen, S. D. Lee: "Regularized learning framework in the estimation of reflectance spectra from camera responses", J. Opt. Soc. Am. A 9, 2673-2683 (2007).

[14] F. H. Imai, R. S. Berns: "Spectral estimation using trichromatic digital cameras", Proceedings of the International Symposium on Multispectral Imaging and Color Reproduction for Digital Archives, Society of Multispectral Imaging of Japan, 1999.

[15] J.E. Jackson: *A User's Guide To Principal Components*, John Wiley & Sons, Inc., 1991.

[16] I. T. Jolliffe: *Principal Component Analysis*, 2nd edition, Springer, 2002 – Verlag New York, Inc., 2002.

[17] K. Kamimura, N. Tsumura, T. Nakaguchi, Y. Miyake: "Evaluation and analysis for spectral reflectance image of human skin", SPIE vol. 5667, 30-37 (2005).

[18] W. Menke: *Geophysical Data Analysis: Discrete Inverse Theory*, Academic Press, Inc., San Diego, 1989.

[19] Y. Murakami, K. Letomi, M. Yamaguchi, N. Ohyama: “Maximum *a posteriori* estimation of spectral reflectance from color image and multipoint spectral measurements”, Appl. Opt. 28, 7068-7082 (2007).

[20] Y. Murakami, T. Obi, M. Yamaguchi, N. Ohyama: “Nonlinear estimation of spectral reflectance based on Gaussian mixture distribution for color image reproduction”, Appl. Opt. 23, 4840-4847 (2002).

[21] W. K. Pratt: *Digital Image Processing*, 3rd edition, Wiley, 2001.

[22] W. K. Pratt, C. E. Mancill: “Spectral estimation techniques for the spectral calibration of a color image scanner”, Appl. Opt. 1, 73-75 (1976).

[23] D. Schweitzer, C. Schrodel, A. Jutte, F. Blaschke, E. Konigsdorffer, W. Visler: “Reflectance spectrophotometry in the human ocular fundus”, Graefes Arch. Clin. Exp. Optalmol 223, 207-210 (1985).

[24] H.-L. Shen, P.-Q. Cai, S.-J. Shao, J.H. Xin: “Reflectance reconstruction for multispectral imaging by adaptive Wiener estimation”, Opt. Express 23, 15545-15554 (2007).

[25] N. Shimano, K.Terai, M. Hironaga: “Recovery of spectral reflectances of objects being imaged by multispectral cameras”, J. Opt. Soc. Am. A 10, 3211-3219 (2007).

[26] N. Shimano: “Recovery of spectral reflectances of objects being imaged without prior knowledge”, IEEE Trans. Image Process. 15, 1848-1856 (2006).

[27] R.T. Smith, T. Nagasaki, J.R. Sparrow, I. Barbazetto, C.CW. Klaver, J.K. Chan: “A Method of Drusen Measurement Based on the Geometry of Fundus Reflectance”, BioMedical Engineering OnLine, 2:10, 2003, at http://www.biomedical-engineering-online.com/content/2/1/10.

[28] M. Sonka, V. Hlavac, R. Boyle: *Image Processing, Analysis, and Machine Vision*, Thomson, 2006.

[29] P. Stigell, K. Miyata, M. Hauta-Kasari: “Wiener estimation method in estimating of spectral reflectance from RGB images”, ISSN 1054-6618, Pattern Recognition and Image Analysis, 2007, Vol. 17, No. 2, 233-242 (2007).

[30] S. Theodoridis, K. Koutroumbas: *Pattern Recognition*, 2nd edition, Elsevier, 2003.

[31] B. A. Wandell: *Foundations of Vision*, Sunderland, Massachusetts, Sinauer Associates, Inc, 1995.

[32] N.P.A. Zagers, D. van Norren: “Absorption of the eye lens and macular pigment derived from the reflectance of cone photoreceptors”, J. Opt. Soc. Am. A 12, 2257-2268 (2004).

APPENDIX 1

Numerical results of PCA approximation of test images with original eigenvectors

Image / # of PC	IMGS2				IMGS2600				IMGS3				IMGS3600			
	Avg. RMSE	Std. RMSE	Max. RMSE	Fidelity	Avg. RMSE	Std. RMSE	Max. RMSE	Fidelity	Avg. RMSE	Std. RMSE	Max. RMSE	Fidelity	Avg. RMSE	Std. RMSE	Max. RMSE	Fidelity
1	0.0081	0.0057	0.0603	0.8341	0.0081	0.0043	0.0444	0.9053	0.0076	0.0044	0.0415	0.9030	0.0073	0.0055	0.0378	0.8903
2	0.0054	0.0046	0.0337	0.9153	0.0038	0.0026	0.0301	0.9754	0.0056	0.0018	0.0166	0.9573	0.0046	0.0016	0.0143	0.9685
3	0.0036	0.0021	0.0298	0.9707	0.0028	0.0014	0.0294	0.9886	0.0039	0.0016	0.0165	0.9776	0.0033	0.0017	0.0142	0.9821
4	0.0029	0.0014	0.0290	0.9826	0.0023	0.0013	0.0271	0.9920	0.0031	0.0010	0.0128	0.9870	0.0022	0.0007	0.0095	0.9928
5	0.0023	0.0012	0.0282	0.9884	0.0020	0.0008	0.0149	0.9945	0.0025	0.0008	0.0127	0.9911	0.0020	0.0006	0.0082	0.9944
6	0.0021	0.0010	0.0238	0.9908	0.0018	0.0008	0.0145	0.9959	0.0020	0.0007	0.0119	0.9946	0.0017	0.0006	0.0080	0.9958
7	0.0019	0.0009	0.0183	0.9928	0.0016	0.0006	0.0097	0.9967	0.0017	0.0006	0.0105	0.9958	0.0015	0.0005	0.0070	0.9966
8	0.0016	0.0008	0.0146	0.9944	0.0014	0.0006	0.0093	0.9973	0.0016	0.0006	0.0090	0.9965	0.0014	0.0005	0.0069	0.9973
9	0.0015	0.0006	0.0108	0.9956	0.0013	0.0005	0.0072	0.9978	0.0014	0.0006	0.0089	0.9972	0.0012	0.0004	0.0065	0.9978
10	0.0014	0.0006	0.0096	0.9963	0.0012	0.0005	0.0072	0.9981	0.0013	0.0005	0.0086	0.9977	0.0011	0.0004	0.0065	0.9983
11	0.0013	0.0005	0.0096	0.9969	0.0011	0.0004	0.0072	0.9984	0.0011	0.0004	0.0082	0.9982	0.0009	0.0004	0.0065	0.9987
12	0.0012	0.0004	0.0071	0.9974	0.0010	0.0004	0.0067	0.9987	0.0010	0.0004	0.0081	0.9986	0.0008	0.0003	0.0051	0.9990
13	0.0011	0.0004	0.0069	0.9978	0.0009	0.0004	0.0067	0.9989	0.0009	0.0004	0.0075	0.9989	0.0007	0.0003	0.0050	0.9993
14	0.0010	0.0004	0.0069	0.9982	0.0008	0.0003	0.0065	0.9991	0.0008	0.0003	0.0065	0.9992	0.0006	0.0003	0.0040	0.9994
15	0.0009	0.0004	0.0066	0.9985	0.0008	0.0003	0.0065	0.9992	0.0006	0.0003	0.0064	0.9994	0.0005	0.0002	0.0040	0.9996

APPENDIX 2

Numerical results of PCA approximation of test images with eigenvectors from the training set

Image / # of PC	IMGS2				IMGS2600				IMGS3				IMGS3600			
	Avg. RMSE	Std. RMSE	Max. RMSE	Fidelity	Avg. RMSE	Std. RMSE	Max. RMSE	Fidelity	Avg. RMSE	Std. RMSE	Max. RMSE	Fidelity	Avg. RMSE	Std. RMSE	Max. RMSE	Fidelity
1	0.0132	0.0072	0.0990	0.9441	0.0144	0.0098	0.0990	0.9441	0.0175	0.0050	0.0335	0.9457	0.0160	0.0046	0.0311	0.9457
2	0.0108	0.0046	0.0541	0.9644	0.0115	0.0051	0.0544	0.9644	0.0148	0.0048	0.0282	0.9659	0.0135	0.0041	0.0239	0.9659
3	0.0070	0.0048	0.0508	0.9780	0.0075	0.0059	0.0508	0.9780	0.0118	0.0033	0.0222	0.9794	0.0110	0.0033	0.0222	0.9794
4	0.0063	0.0034	0.0416	0.9841	0.0068	0.0042	0.0416	0.9841	0.0109	0.0030	0.0195	0.9854	0.0100	0.0028	0.0175	0.9854
5	0.0061	0.0032	0.0398	0.9886	0.0066	0.0041	0.0398	0.9886	0.0100	0.0026	0.0173	0.9898	0.0093	0.0026	0.0173	0.9898
6	0.0054	0.0027	0.0348	0.9919	0.0060	0.0034	0.0348	0.9919	0.0089	0.0023	0.0163	0.9931	0.0085	0.0025	0.0163	0.9931
7	0.0051	0.0025	0.0348	0.9938	0.0058	0.0032	0.0348	0.9938	0.0084	0.0020	0.0157	0.9946	0.0082	0.0023	0.0157	0.9946
8	0.0049	0.0025	0.0342	0.9953	0.0056	0.0031	0.0342	0.9953	0.0080	0.0020	0.0157	0.9959	0.0079	0.0023	0.0157	0.9959
9	0.0048	0.0025	0.0341	0.9963	0.0055	0.0031	0.0341	0.9963	0.0072	0.0017	0.0155	0.9969	0.0072	0.0019	0.0155	0.9969
10	0.0046	0.0025	0.0341	0.9972	0.0052	0.0032	0.0341	0.9972	0.0071	0.0016	0.0153	0.9976	0.0071	0.0019	0.0153	0.9976
11	0.0040	0.0021	0.0330	0.9977	0.0045	0.0025	0.0330	0.9977	0.0068	0.0018	0.0151	0.9982	0.0070	0.0021	0.0151	0.9982
12	0.0039	0.0019	0.0240	0.9982	0.0043	0.0021	0.0240	0.9982	0.0037	0.0013	0.0104	0.9985	0.0033	0.0009	0.0089	0.9985
13	0.0038	0.0019	0.0239	0.9985	0.0042	0.0021	0.0240	0.9985	0.0034	0.0011	0.0099	0.9989	0.0031	0.0009	0.0082	0.9989
14	0.0036	0.0018	0.0234	0.9988	0.0040	0.0020	0.0234	0.9988	0.0031	0.0011	0.0097	0.9991	0.0027	0.0007	0.0074	0.9991
15	0.0035	0.0017	0.0221	0.9990	0.0039	0.0019	0.0221	0.9990	0.0027	0.0009	0.0085	0.9993	0.0026	0.0007	0.0073	0.9993